Verônica Miquelin Machado

Effect of elastic-plastic stress in the defect tolerance under stress corrosion cracking

DISSERTAÇÃO DE MESTRADO

DEPARTAMENTO DE ENGENHARIA MECÂNICA

Programa de Pós-Graduação em Engenharia Mecânica

Rio de Janeiro
May 2016

Pontifícia Universidade Católica
do Rio de Janeiro

Verônica Miquelin Machado

Effect of elastic-plastic stress in the defect tolerance under stress corrosion cracking

DISSERTAÇÃO DE MESTRADO

Dissertation presented to the Programa de Pós-Graduação em Engenharia Mecânica of the Departamento de Engenharia Mecânica do Centro Técnico Científico da PUC–Rio, as partial fulfilment of the requirements for the degree of Mestre em Engenharia Mecânica.

Advisor: Prof. Jaime Tupiassú Pinho de Castro

Rio de Janeiro
May 2016

Pontifícia Universidade Católica
do Rio de Janeiro

Verônica Miquelin Machado

Effect of elastic-plastic stress in the defect tolerance under stress corrosion cracking

Dissertation presented to the Programa de Pós-Graduação em Engenharia Mecânica of the Departamento de Engenharia Mecânica do Centro Técnico Científico da PUC–Rio , as partial fulfillment of the requirements for the degree of Mestre

Prof. Jaime Tupiassú Pinho de Castro
Advisor
Departamento de Engenharia Mecânica - PUC-Rio

Prof. Marco Antonio Meggiolaro
Departamento de Engenharia Mecânica - PUC-Rio

Prof. José Luiz de França Freire
Departamento de Engenharia Mecânica - PUC-Rio

Márcio da Silveira Carvalho
Coordinator of the Centro Técnico Científico da PUC-Rio

Rio de Janeiro, May 4th, 2016

Verônica Miquelin Machado

Graduated in Mechanic and Army Engineering at Instituto Militar de Engenharia (IME - Rio de Janeiro, Brazil) in 2010. Currently works in the Metallic Materials research department at Technip Brazil

Bibliographic data

Machado, Verônica Miquelin

Effect of elastic-plastic stress in the defect tolerance under stress corrosion cracking / Verônica Miquelin Machado; advisor: Jaime Tupiassú Pinho de Castro. — 2016.

101 f: il. color ; 30 cm

Dissertação (mestrado) - da PUC-Rio, Departamento de Engenharia Mecânica,2016.

Inclui bibliografia

1. Engenharia Mecânica – Teses. 2. Mecânica da Fratura elasto-plástica. 3. Trincas curtas. 4. Integral J. 5. Tensão residual. 6. Corrosão sob tensão. I. Castro, Jaime Tupiassú Pinho de. II. da PUC-Rio. Departamento de Engenharia Mecânica. III. Título.

CDD: 621

Acknowledgments

To my husband Luiz Felippe for the love and motivation.

To my parents for the education.

To my advisor by the knowledge shared.

To all LabH2S-INT person, in special Rodrigo Landim for the support in the experiments.

To Technip for the trust and support.

Abstract

Machado, Verônica Miquelin; Castro, Jaime Tupiassú Pinho de (Advisor). **Effect of elastic-plastic stress in the defect tolerance under stress corrosion cracking**. Rio de Janeiro, 2016. 101p. MSc. Dissertation - Departamento de Engenharia Mecânica, Pontifícia Universidade Católica do Rio de Janeiro.

Stress Corrosion Cracking (SCC), which consist in the initiation and propagation of cracks due to the combined attack of mechanical stresses and a corrosive environment is a potential danger for structures and components. Moreover, SCC can be explained by different mechanisms depending on the metal environmental pair, what makes difficult to create a generalized analytical approach to predict the crack behavior in SCC. Therefore, projects often use an over-conservative design criteria that disqualify a material susceptible to SCC without properly evaluate the influence of the stress fields that drive them. The aim of this work is to evaluate the effect of elastic-plastic stress in SCC. This mechanical approach assumes that all chemical effects involved in SCC problems can be appositely described and quantified by additional material resistances to crack initiation and propagation at under specific environment. Aluminum bending specimens in Gallium environment are used to predict the effect of the residual stress induced by plastic deformation in the crack initiation under SCC conditions. Furthermore, a quantitative analysis based on the non-propagating crack behavior departing from notch tips are used to calculate the necessary stress to initiate and propagate SCC in AISI 4140 steel notched specimens under aqueous hydrogen sulfide environment. The non-propagating crack behavior and the maximum load supported by notched specimens are analyzed under linear elastic and elastic-plastic stress field through the proposed model that will be validated by experimental data.

Keywords

Elastic plastic stress field; Short Crack; J-integral; Residual stress; Stress corrosion cracking.

Resumo

Machado, Verônica Miquelin; Castro, Jaime Tupiassú Pinho de. **Efeito de tensões elastoplásticas à tolerância de defeitos em corrosão sob tensão**. Rio de Janeiro, 2016. 101p. Dissertação de Mestrado — Departamento de Engenharia Mecânica, Pontifícia Universidade Católica do Rio de Janeiro.

Corrosão sob tensão (SCC), que consiste na iniciação e propagação de trincas devido ao efeito combinado de tensões mecânicas e o ambiente corrosivo, é um dano potencial para estruturas e componentes. Além do mais, SCC pode ser explicado por diferentes mecanismos dependendo do par material ambiente corrosivo considerado, o que dificulta o uso de um modelo geral para predizer o comportamento de trincas em SCC. Sendo assim, projetos frequentemente utilizam um critério conservativo que desqualifica materiais susceptíveis à SCC sem analisar de maneira apropriada a influência dos campos de tensão que a induzem. O objetivo deste trabalho é avaliar o efeito de tensões elastoplásticas na corrosão sob tensão. Esta abordagem mecânica considera que todos os efeitos corrosivos envolvidos na corrosão sob tensão podem ser apropriadamente quantificados pelas tradicionais resistências do material à iniciação e propagação de trincas para um ambiente corrosivo específico. Corpos de prova de flexão em Alumínio fragilizados por Gálio líquido serão utilizados para prever o efeito de tensões residuais induzidas por deformações plásticas na iniciação de trincas por corrosão sob tensão. Além disso, uma análise quantitativa baseada no comportamento de trincas não propagantes a partir de entalhes será usada para estimar a tensão necessária para iniciar e propagar trincas em corpos de prova entalhados em aço AISI 4140 sujeitos à corrosão por sulfeto de hidrogênio em ambiente aquoso. O comportamento de trincas curtas e a carga máxima suportada pelos corpos de prova entalhados são analisadas considerando campos de tensões lineares elástico e elastoplásticos através do modelo proposto que será validado através de dados experimentais.

Palavras Chave

Mecânica da Fratura elasto-plástica; Trincas curtas; Integral J; Tensão residual; Corrosão sob tensão.

Contents

List of Figures

List of Tables

List of Symbols

Symbol	Description
a	Crack length
$a0$	Incremental short crack length
A	Area
b	Initial notch size or Ellipse major axis
B	Specimen thickness
c	Ellipse minor axis
CP	Specimen
CT	Compact Tension
DCT	Disc Compact Tension
E	Modulus of Elasticity
EAC	Environmental Assisted Cracking
E_p	Potential Energy
F	Geometric constant
FEA	Finite Element Analysis
g	non-dimensional function
G	Griffth strain energy released rate
G_{IC}	Critical Griffth strain energy released rate
h_b	Ramberg-Osgood coefficient
H_b	Ramberg-Osgood coefficient
I	Moment of Inertia
J	J-integral
J_{el}	Elastic part of J-integral
J_{long}	J-integral considering long crack behaviour
J_{pl}	Plastic part of J-integral
J_{short}	J-integral considering short crack behaviour
J_{SCC}	J-integral threshold under SCC condition
J_{th}	J-integral threshold
K	Amplitude of singularity
K_I	Stress Intensity Factor at mode I
K_{IC}	Critical Stress Intensity Factor

K_{SCC}	Stress Intensity Factor threshold under SCC condition
k_t	Stress Concentration Factor
k_ε	Strain Concentration Factor
k_σ	Stress Concentration Factor
L	Length
LME	Liquid Metal Embrittlement
M	Moment
M_E	Moment at yielding
n	Hardening coefficient/ normal vector
P	Load
P_{break}	Break Load
P_c	Loading
P_E	Load at yielding
r	Cylindrical coordinate - radial distance
R	Radius
SCC	Stress Corrosion Cracking
SCF	Stress Concentration Factor
S_{SCC}	Stress threshold under SCC condition
t	Thickness
T	Traction
u	Displacement
W	Specimen size
W_e	Elastic Strain Energy
W_p	Plastic Strain Energy
W_ε	Strain Energy
x	Cartesian coordinate
y	Cartesian coordinate
y_E	Section length at yielding
α	Coefficient
δ_{SCC}	Crack Opening Displacement under SCC condition
ΔJ_{short}	J-integral range considering short behavior
ΔK	Stress Intensity Factor Range
ΔK_{th}	Stress Intensity Factor Threshold
$\Delta K_{th-short}$	Stress Intensity Factor Threshold considering short crack behavior
$\Delta K_{th-long}$	Stress Intensity Factor Threshold considering long crack behavior

ΔK_{short}	Stress Intensity Factor Range considering short behavior
$\Delta K_{\varepsilon-short}$	Strain Intensity Factor Range considering short crack behavior
$\Delta K_{\sigma-short}$	Stress Intensity Factor Range considering short crack behavior
$\Delta\varepsilon$	Strain Range
$\Delta\sigma$	Stress Range
$\Delta\sigma_l$	Fatigue Limit
ε	Strain
ε^p	Plastic Strain
ε_0	Strain Factor
ε_{break}	Break Strain
ε_E	Strain at yielding
ε_d	Unloading Strain
ε_{max}	Maximum Strain
ε_{res}	Residual Strain
Γ	Curve Surrounding notch tip
η	Free surface factor
ϕ	Stress gradient
ν	Poisson coefficient
θ	Cylindrical coordinate - angle
ρ	Notch radius
σ	Stress
σ_0	Stress Factor
σ_{break}	Break Stress
σ_d	Unloading Stress
σ_{max}	Maximum Stress
σ_n	Normal Stress
σ_{y0}	Yielding Stress
τ	Shear stress

1
Introduction

Stress corrosion cracking (SCC), which consists of the initiation and propagation of cracks due to the combined and synergistic attack of mechanical stresses and a corrosive environment, is a potential danger for structures and components [1].

As examples of SCC failures, it may be mention the catastrophic failure of an aluminum alloy used in an aircraft structure, the explosion of boilers, the ruptures of liquid or gas transmission pipes, the chloride intergranular corrosion occurring in austenitic stainless steel which is of a great concern for the nuclear industry, the caustic SCC observed on tubing made from the Inconel alloy of boiler feed waters among numerous other examples [2].

SCC is a time dependent phenomenon, controlled by microstructural and metallurgical features and by localized electrochemical processes at the crack tip. Because of that, a generalized analytical approach based on micromechanics and physical metallurgy that would allow predicting the crack behavior in SCC is arduous.

Therefore, an over-conservative design criterion which disqualifies a material susceptible to SCC without properly evaluate the influence of the stress fields that drive them, is usual in practice.

On the other hand, structural integrity assessment procedure must include proper stress analysis techniques. The criteria for the stresses are simply that they be tensile and of sufficient magnitude. These stresses may be due to any source: applied, residual, thermal or welding, since numerous cases of SCC have been observed with no externally applied stresses [3].

That is why a mechanical approach based on a fracture mechanics can provide insights into the phenomenon of SCC and help to develop guidance for avoiding or controlling SCC during service, and to reduce the likelihood of unexpected failure caused by SCC [1].

This mechanical approach assumes that all chemical effects involved in SCC problems can be appositely described and quantified by the traditional material resistances to crack initiation (S_{SCC}) and propagation (K_{SCC} and J_{SCC}) under fixed environments. The material properties considering the SCC are well accepted by

the industry since there are codes to measure them, such as the ASTM E1681 [4] to measure K_{SCC} and the ASTM F1624 [5] used to measure S_{SCC} under hydrogen environment.

This macro-mechanical methodology of use fracture mechanics extended to the SCC is already being used.

Dietzel [1] obtained data from fracture mechanics based on SCC tests to evaluate critical loads and remaining lifetimes of pre-cracked components in aggressive environments and yield information about the efficiency of countermeasures and protection means.

Moreover, Dietzel *et al.* [6] investigated the SCC of 2024 T351 Aluminum alloy in an aqueous 3.5% sodium chloride solution environment using three fracture mechanics based testing techniques: constant load, constant displacement and displacement rate to evaluate the K_{SCC}, J_{SCC} and δ_{SCC} parameters, and they use the linear-elastic and elastic-plastic fracture mechanics to discuss a criteria for the accelerated evaluation of SCC.

Peng *et al.* [7] determined quantitatively the SCC growth rate of stainless steel in high temperature oxygenated water using a fundamental crack tip strain rate equation derived from the time-based mathematical derivation of continuum mechanics equation.

Abramson *et al.* [8] ascertained crack growth resistance curves for the stress corrosion cracking of two magnesium alloys in which the J-integral is plotted against the crack extension.

More specifically, the short crack behavior under SCC have been studied by Sadananda and Vasudevan [9] where a failure diagram for a given material and environment system defines conditions under which a crack initiated at the threshold stress in a smooth specimen becomes a propagating crack, by satisfying the threshold stress intensity of a long crack, or non-propagating conditions prevails.

EPRI [10] reviews current knowledge of environmentally assisted cracking (EAC) initiation and short crack growth (by stress corrosion cracking, strain induced corrosion cracking, and, to a lesser extent, corrosion fatigue) in nickel base alloys, austenitic stainless steels, and carbon and low-alloy steels exposed to typical pressurized water reactor and boiling water reactor aqueous environments.

The present work aims to develop a mechanical approach for the SCC phenomena that are capable to evaluate the resistance of a structure under SCC conditions through the stress field analysis.

The work is broken in two fronts. The first is a continuation of the work about notch sensitivity factor using the short crack threshold [11] [12] [13] that was extended to the stress corrosion cracking problem.

The short crack behavior and notch sensitivity effects are already studied in

environmentally assisted cracking at the linear elastic regime in Aluminum Gallium metal environment pair [14] and at steel hydrogen sulfide metal environment pair [15].

In this work, this evaluation is extended to short crack behavior under linear elastic regime using notched compact tension specimen in steel under hydrogen sulfide environment in an attempt to demonstrate more quantitatively the effectiveness of the proposed model.

Further, the proposed model is extended to the elastic-plastic regime. Then, an elastic-plastic model to predicted the short crack behavior of stress corrosion cracks in compact specimens is proposed and the methodology is verified through experiments in steel hydrogen sulfide material environment pair.

The second front is an evaluation of the effect of residual stress on stress corrosion cracking resistance. In this work, bending specimens of Aluminum alloy with controlled induced residual stress by plastic deformation is analyzed regarding the stress corrosion cracking resistance in Gallium environment.

Therefore the present work is divided into six chapters. Chapter 1 is this introduction whereas the chapter 2 aims to describe the theoretical concepts necessary to develop the models.

Section 2.1 introduce the concept of stress concentration factor from notches and the analytical solutions from Kirsh, Inglis and Creager and Paris are detailed.

Moreover, section 2.2 shows the models considered to describe the stress and strain field around a crack tip. In this section the crack driving force denoted by the strain energy released rate (G) proposed by Griffith, the stress intensity factor (K_I) proposed by Irwin and the J-integral defined by Rice are analyzed. Furthermore, the J-integral simplification proposed by Hutchinson is described.

Section 2.3 describes the short crack model at linear elastic regime considering the Topper *et al.* [16][17] definition and expanding the idea for the short cracks from notched specimens, whereas section 2.4, as the previous section, shows the short crack model at the elastic-plastic regime.

Section 2.5 presents stress corrosion cracking overview and specifically the LME by Aluminum in Gallium and the stress corrosion of steel under hydrogen sulfide particularities.

Finally , section 2.6 present the residual stress theory.

Chapter 3 describes the numerical models adopted in this work. Section 3.1 describes the particularities of the finite element method used to extract the stress intensity factor in the linear-elastic regime of the compact specimen when the crack growths from the notch and the J-integral in the elastic-plastic regime also with the crack length. Moreover, section 3.2 presents the model used to predict the residual stress imposed in the bending specimens due to plastic deformation.

Chapter 4 describes the material properties and experimental procedures. Section 4.1 describes the experimental procedure to validate the short crack from notched specimens experiments using AISI 4140 steel in aqueous hydrogen sulfide environment. Whereas, section 4.2 describes the experimental procedure used to validate the effect of residual stress in the stress corrosion cracking susceptibility in Aluminum Gallium material environment pair.

The results are presented on section 5, with section 5.1 detailing the model and experimental results in steel and hydrogen sulfide of the short crack from notched specimens at the linear-elastic and elastic-plastic regime and section 5.2 detailing the residual stress model and experimental results of Aluminum in Gallium for the effect of residual stress in SCC.

To end the present work, section 6 brings the conclusions and future works that can be carried out to continuous this research.

2
Theoretical Concepts

2.1
Stress Concentration Factor

As published by Saint-Venant in 1855,

> "... the difference between the effects of two different but statically equivalent loads becomes very small at sufficiently large distances from the load."

means that near load application, notches, geometry transitions, the classic solution from the theory of elasticity it is not valid to estimate the stresses in the structure. However, generally, the structure maximum stress is at these singular locations, making necessary to estimate the real stress at these locations.

2.1.1
The Kirsh hole

The first analytical solution for the real stress in a structure unique location was proposed by Kirsch in 1898, where the stress around a circular hole in an infinite plate, as represented in figure 2.1 was estimated.

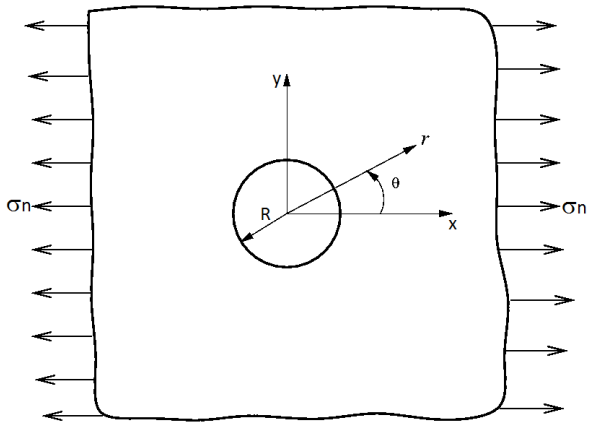

Figure 2.1: Infinite Plate with hole analyzed by Kirsch

The equations for the stress field around the hole is given by equation 2.1 [18].

$$\begin{cases} \sigma_\theta = (\sigma_n/2)[(1+R^2/r^2) - (1+3R^4/r^4)\cos(2\theta)] \\ \sigma_r = (\sigma_n/2)[(1-R^2/r^2) + (1-4R^2/r^2+3R^4/r^4)\cos(2\theta)] \\ \tau_{r\theta} = -(\sigma_n/2)[(1+2R^2/r^2-3R^4/r^4)\sin(2\theta)] \end{cases} \tag{2.1}$$

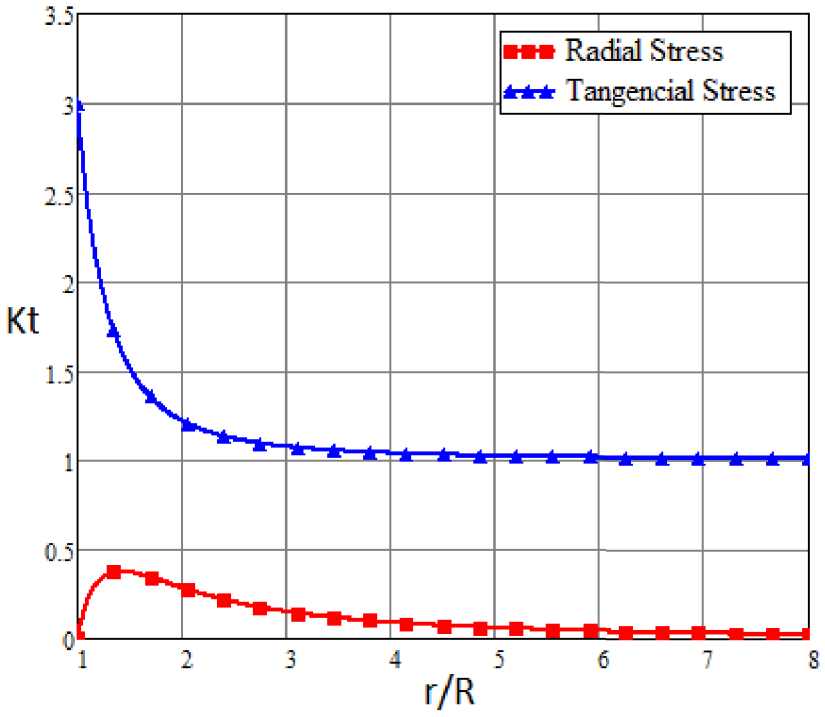

Figure 2.2: Stress concentration factor from Kirsch equations

Figure 2.2 presents the stress concentration factor for the radial and tangential stress calculated using the Kirsch equations for a position 90 degrees from the applied stress direction.

It can be noted that the stress concentration factor for the tangential stress is equal to 3 on the border of the hole and decrease until reach 1 at a distance approximately five times the hole radius. In other words, the stress applied to the plate with a hole is magnified by 3 on the hole border and decay to the real apply load far from the border.

However, as the Kirsch equations are a function of the angle θ, the stress magnification is not uniform around the hole. The maximum stress magnification equal to 3 is at 90 degrees from applied stress direction. Figure 2.3 below, shows the stress concentration factor distribution around the hole border with the angle θ.

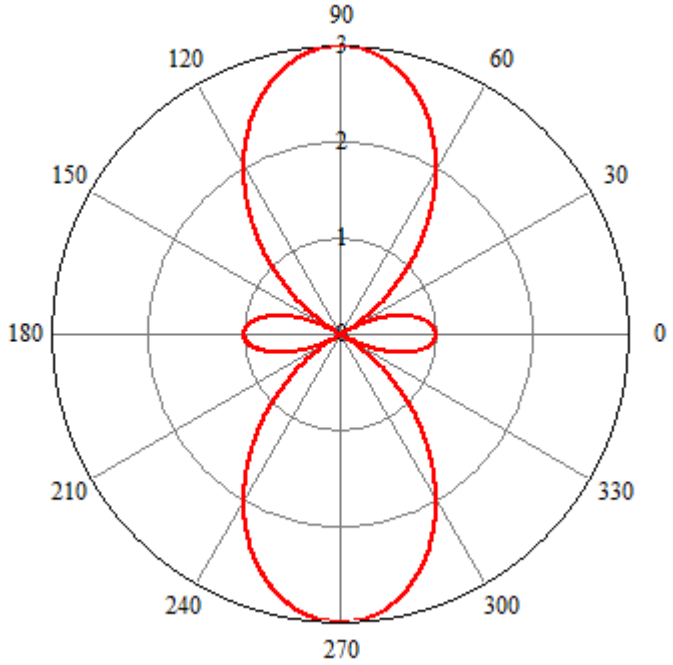

Figure 2.3: Stress concentration distribution around Kirsch hole

2.1.2 The Inglis hole

Similar to the Kirsch solution for stress concentration factor around a circular hole in an infinite plate, Inglis propose a more generic analytical solution to describe the stress concentration factor around an ellipse in an infinite plate. Figure 2.4 presents the Inglis problem.

The equation 2.2, presents the stress concentration factor for the normal stress (σ_y) at x distance from the ellipse center as shown in the figure 2.4 [18].

$$\varphi(x,b,c) = 1 + \frac{[(b^2-2bc).[x-(x^2-b^2+c^2)^{0.5}].(x^2-b^2+c^2)+b.c^2.(b-c).x]}{(b-c)^2.(x^2-b^2+c^2).(x^2-b^2+c^2)^{0.5}} \tag{2.2}$$

The maximum stress is found to be in the border of the major ellipse axis where $x = b$, and then replacing in equation 2.3, the stress concentration factor from an ellipse hole in an infinite plate is:

$$k_t = 1 + 2.\frac{b}{c} \tag{2.3}$$

Figure 2.5 presents the stress concentration factor for different ellipses as a

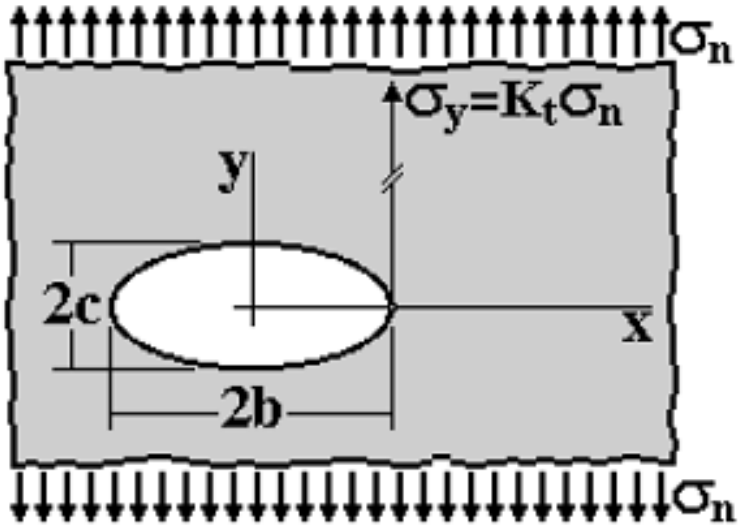

Figure 2.4: The Inglis problem

function of the distance x from the major axis and perpendicular to the applied stress as presented in figure 2.4.

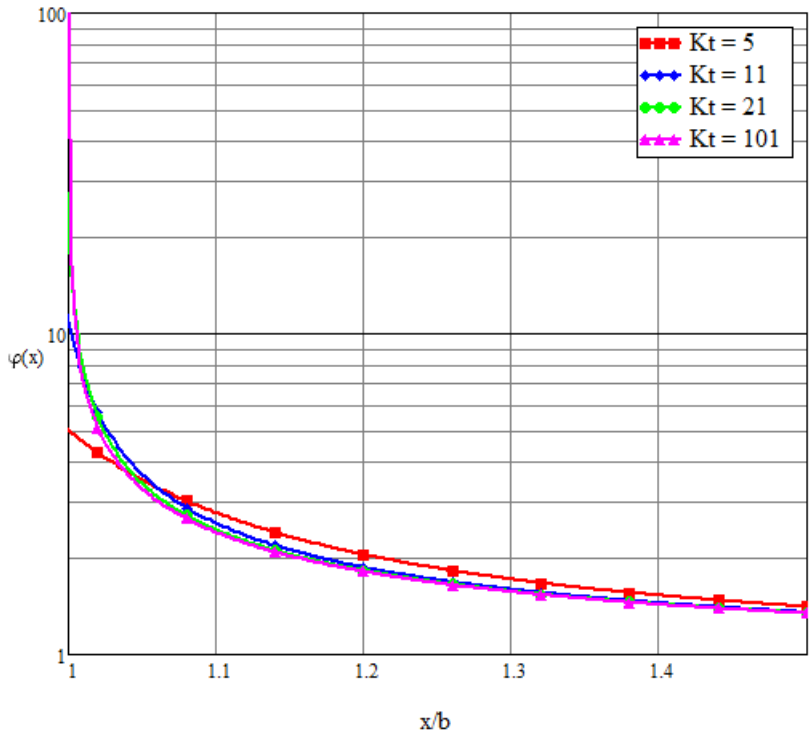

Figure 2.5: Stress concentration factor for different ellipses

The four ellipses considered have major axis equal to 10*mm* and minor axis equal to 5*mm*, 2*mm*, 1*mm* and 0.2*mm* resulting in a stress intensity factor equal to 5,11,21 and 101 respectively in accordance with equation 2.3.

Is interesting to note that after a small length in front of the elliptical hole, there is no difference between the ellipses hole analyzed and therefore the stress gradient near the hole is very high mainly for the sharpest ellipses with high k_t.

2.1.3 Creager and Paris

The analytical solutions for the stress concentration field around a notch are not available for too much different geometries as for the circular hole and ellipse at an infinite plate shown in above section.

Because of this, Creager and Paris developed a methodology to estimate the stress concentration field based on the stress intensity factor which is tabulated for more geometries as in reference [19].

The stress intensity factor K_I is capable of defining the stress field near the crack tip as shown in equation 2.4 for mode I [18].

$$\begin{Bmatrix} \sigma_x \\ \sigma_y \\ \tau_{xy} \end{Bmatrix} = \frac{K_I}{\sqrt{2\pi r}} . \frac{\rho}{2r} \begin{Bmatrix} -\cos(3\theta/2) \\ \cos(3\theta/2) \\ -\sin(3\theta/2) \end{Bmatrix} + \frac{K_I}{\sqrt{2\pi r}} . \cos(\theta/2) \begin{Bmatrix} 1-\sin(\theta/2)\sin(3\theta/2) \\ 1+\sin(\theta/2)\sin(3\theta/2) \\ \sin(\theta/2)\cos(3\theta/2) \end{Bmatrix} \tag{2.4}$$

In this methodology, the stress concentration field is estimated based on stress intensity field considering the origin of axis displaced of $\rho/2$ to the notch. So, the stress field around a notch will be described by equation 2.5 and $r = x + \rho/2$, where x is the horizontal distance from the notched border.

$$\begin{Bmatrix} \sigma_x \\ \sigma_y \\ \tau_{xy} \end{Bmatrix} = \frac{K_I}{\sqrt{\pi(2x+\rho)}} . \frac{\rho}{(2x+\rho)} \begin{Bmatrix} -\cos(3\theta/2) \\ \cos(3\theta/2) \\ -\sin(3\theta/2) \end{Bmatrix} + \frac{K_I}{\sqrt{\pi(2x+\rho)}} . \cos(\theta/2) \begin{Bmatrix} 1-\sin(\theta/2)\sin(3\theta/2) \\ 1+\sin(\theta/2)\sin(3\theta/2) \\ \sin(\theta/2)\cos(3\theta/2) \end{Bmatrix} \tag{2.5}$$

Considering the σ_y at $\theta = 0$,

$$\sigma_y = \frac{K_I}{\sqrt{\pi(2x+\rho)}} . \left(\frac{\rho}{(2x+\rho)} + 1\right) \tag{2.6}$$

2.2 Crack Driving Force

Based on the stress concentration factor theory presented in section 2.1, the problem of stress and strain fields at a crack tip results in a mathematical singularity, since a crack is modeled as a notch with radius $\rho \quad 0$.

To disregard this singularity of the stress and strain fields, in 1920 Griffth deals with the fracture mechanic issue using an energy based analysis, and then introduce the quantity G, which represents the strain energy released as the crack growths as per equation 2.7.

$$G = -\frac{\partial E_p}{\partial A} \tag{2.7}$$

This quantity is useful to predict a failure when G is greater than a critical energy G_{IC} which is a material property, that is $G > G_{IC}$.

However, since the analytical assessment of the elastic energy stored is laborious, the use of the Griffith theory was impractical at that time. Therefore, to solve this issue, Irwin introduce the concept of stress intensity factor which describes the stress field around a crack as per equation 2.8.

$$\begin{Bmatrix} \sigma_x \\ \sigma_y \\ \tau_{xy} \end{Bmatrix} = \frac{K_I}{\sqrt{2\pi r}}.\cos(\theta/2) \begin{Bmatrix} 1-\sin(\theta/2)\sin(3\theta/2) \\ 1+\sin(\theta/2)\sin(3\theta/2) \\ \sin(\theta/2)\cos(3\theta/2) \end{Bmatrix} \tag{2.8}$$

Where the stress intensity factor K_I is function of the applied load far from the crack, the geometry of the component and the crack size a as per equation 2.9.

$$K_I = \sigma \quad \sqrt{\pi a} f(a/W) \tag{2.9}$$

Equations similar to 2.8 can be written for mode II and III of loading.

The stress intensity factor formulation was very well accepted by the industry and still be very useful nowadays. However, this theory is limited to the linear elastic fracture mechanics and only small scale yielding near the crack tip is acceptable.

The small scale yielding is the case where the yielded zone near the tip is small in size compared to the geometric dimensions. There are lots of criteria to define the small scale yielding validity, the criteria considered in this work is the ASTM E399 [20] criteria defined in equation 2.10

$$\begin{Bmatrix} B \\ a \\ W-a \end{Bmatrix} > 2.5(K_{IC}/\sigma_{y0})^2 \tag{2.10}$$

However, in the elastic-plastic regime, where the stress intensity factor can not be used, the J-integral formulation proposed by Rice [21] is used to model the elastic-plastic behavior of metals in relation to fracture.

The elastic-plastic behavior of metals is best modelled through incremental stress-strain relations, but there is no a path integral formulation for the incremental plasticity, and then, the deformation plasticity, which is the material modelled as non-linear elastic material with a linear Hookean response for stress states within a yield surface and a non-linear hardening response for those outside, is considered.

However, as in elastic-plastic materials both the crack tip propagation and the plastic deformation dissipate energy, the deformation plasticity model should be used carefully to evaluate the J-integral due to the crack propagation.

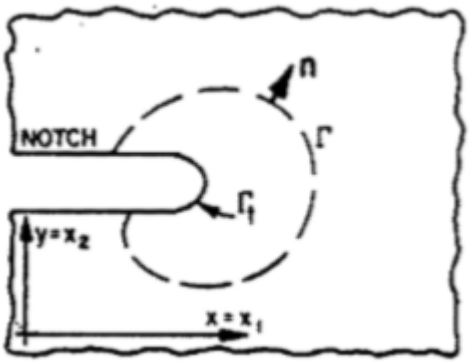

Figure 2.6: J-integral around a notch tip. [21]

The J-integral is defined by equation 2.11.

$$J = \int_{\Gamma} (W_{\varepsilon} dy - T \frac{\partial u}{\partial x} ds) \tag{2.11}$$

Where,
Γ is a curve surrounding the notch tip as per figure 2.6;
T is the traction vector defined according to the outward normal along Γ;

$$T_i = \sigma_{ij}.n_j \tag{2.12}$$

u is the displacement vector;
ds is the element of arc along Γ;
W_{ε} is the strain energy density defined in equation 2.13;

$$W_{\varepsilon} = \int_0^{\varepsilon} \sigma_{ij} d\varepsilon_{ij} \tag{2.13}$$

This formulation has interesting properties, among them:
$J = 0$ for any closed curve Γ;

J is path independent, that is, J has the same value when computed by integrating along either Γ_1 or Γ_2, where Γ_1 and Γ_2 are any two paths surrounding the notch tip;

$T = 0$ and $dy = 0$ on the portions of the path along the notch surface. So, taking Γ_t, as per figure 2.6, close to the notch tip we can make the J-integral dependent only on the local field as represented by equation 2.14 and we can conclude that J-integral is an averaged measure of the strain on the notch tip.

$$J = \int_{\Gamma_t} W_\varepsilon dy \tag{2.14}$$

The application to the J-integral to the crack problems reveals that the strain energy density must have an exact $1/r$ variation as the crack tip is approached, and the stress, strain and displacement fields associated with the dominant singularity are defined by equation 2.15. [22]

$$\begin{cases} \sigma_{ij}(r,\theta) = Kr^{-1/(n+1)}\hat{\sigma}_{ij}(\theta) \\ \varepsilon^p_{ij}(r,\theta) = \alpha K^n r^{-n/(n+1)}\hat{\varepsilon}^p_{ij}(\theta) \\ u_i(r,\theta) = \alpha K^n r^{1/(n+1)}\hat{u}_i(\theta) \end{cases} \tag{2.15}$$

Where,

r is the distance from the crack tip;

θ is the angle measured from directly ahead of the crack;

$\hat{\sigma}_{ij}(\theta), \varepsilon^p_{ij}(\theta)$ and $\hat{u}_i(\theta)$ are the dimensionless functions depends on the strain hardening exponent n;

K is the amplitude of the singularity.

When small scale yielding pertains, J related to the elastic stress intensity factor (K_I) by a simple formula is given by equation 2.16 in plane strain condition.

$$J = \frac{K_I^2(1-\nu^2)}{E} \tag{2.16}$$

For large scale yielding, J cannot be simply calculated in general, since it depends on a complicated way on the geometry, load level and non-linear stress-strain behavior.

However, Hutchinson [23] formulates a simple and functional relationship between J and the applied load quantity for the particular case of plane strain problem, material modeling as pure power hardening relations, mode I loading and

stress field symmetric with respect to the crack. This formulation are presented in equation 2.17.

$$J = \alpha\sigma_0\varepsilon_0 a(\sigma/\sigma_0)^{n+1}\hat{J}(a/b,n) \tag{2.17}$$

2.3 Short Crack at Linear Elastic Regime

It is known that the fatigue cracks usually initiate at geometric discontinuities due to a high level of stress at the notch roots. Due to the stress concentration factor, the crack will form quickly at the root of the sharp notch where the stress level is high, but they could not continue to grow across the specimen cross section where the effect of notch SCF can be disregarded and then the stress is low, generating a non-propagating crack.

The non-propagating crack at linear-elastic regime is studied through the fatigue short crack model proposed by El-Haddad, Topper and Smith [16]. In this model, since the plasticity effect in the crack tip is to increase the stress concentration factor above the elastic solutions near the notch, the short cracks are modeled with an effective length as shown in equation 2.18.

$$a_{effective} = a + a_0 \tag{2.18}$$

And then, the strain intensity factor is represented by equation 2.19.

$$\Delta K_{\varepsilon-short} = E\Delta\varepsilon\sqrt{\pi(a+a_0)} \tag{2.19}$$

At elastic regime, equation 2.20 can be considered.

$$\Delta K_{\sigma-short} = \Delta\sigma\sqrt{\pi(a+a_0)} \tag{2.20}$$

For short non-propagating cracks, a 0, the stress intensity factor threshold (ΔK_{th}) corresponds to the stress equal to the fatigue limit of the material ($\Delta\sigma_l$). Therefore, the short crack characteristic length can be defined as a material property as follow by the equation 2.22.

$$\Delta K_{th} = \Delta\sigma_l \quad \overline{\pi a_0} \tag{2.21}$$

$$a_0 = \frac{1}{\pi}\left(\frac{\Delta K_{th}}{\Delta\sigma_l}\right)^2 \tag{2.22}$$

The short cracks at notches are analyzed in accordance with equation 2.23 also in reference [16].

$$\Delta K_{\varepsilon-short} = E k_{\varepsilon} \Delta\varepsilon \sqrt{\pi(a+a_0)} \tag{2.23}$$

Where in the elastic regime, the strain concentration factor is equal to the stress concentration factor, $k_{\varepsilon} = k_t$, resulting in equation 2.24.

$$\Delta K_{short} = k_t \Delta\sigma \sqrt{\frac{a_0 \pi(a+a_0)}{a_0}} \tag{2.24}$$

$$\frac{\Delta K_{short}}{\Delta\sigma \quad \overline{\pi a_0}} = k_t \sqrt{\frac{a+a_0}{a_0}} \tag{2.25}$$

Figure 2.7 plots the curve of short stress intensity factor vs. crack length in a non-dimensional form described by equation 2.25.

In this figure, the non-dimensional crack stress intensity factor from elliptical notches is plotted. The red curve ($k_t = 3$) is the non-dimensional ΔK_{short} from an elliptical notch with semi-axis $b = 10mm$ and $c = 10mm$, which corresponds to a circular notch with 10mm radius, whereas the blue curve ($k_t = 101$) and the green curve (Long crack $k_t = 101$) are from an elliptical notch with semi-axis $b = 10mm$ and $c = 0.2mm$, which results in a $k_t = 101$ and a notch radius equal to $\rho = 4.10^{-3}mm$.

From figure 2.7, for the sharp notch, the short stress intensity factor starts at a high value and then first decrease until a minimum value to after some crack length increase with a, whereas for a long crack model and short crack model of blunt notches the stress intensity factor always increase with crack length. The non-propagating crack behavior can occur only in the sharp notches modeled with the short crack behavior, where the stress intensity factor first decrease with crack length. So, there is a limit condition for the notch radius to generate non-propagating cracks.

The stress concentration factor k_t at equation 2.24 can be split into η which is the free surface factor and $\varphi(a)$ which represents the stress gradient near the notch root described in detail in section 2.1.

$$k_t = \eta.\varphi(a) \tag{2.26}$$

Comparing the original stress intensity factor threshold defined for long cracks with the threshold defined to describe short cracks behavior we have:

$$\Delta K_{th-long} = \eta\,\varphi(a)\Delta\sigma_{th} \quad \overline{\pi a} \tag{2.27}$$

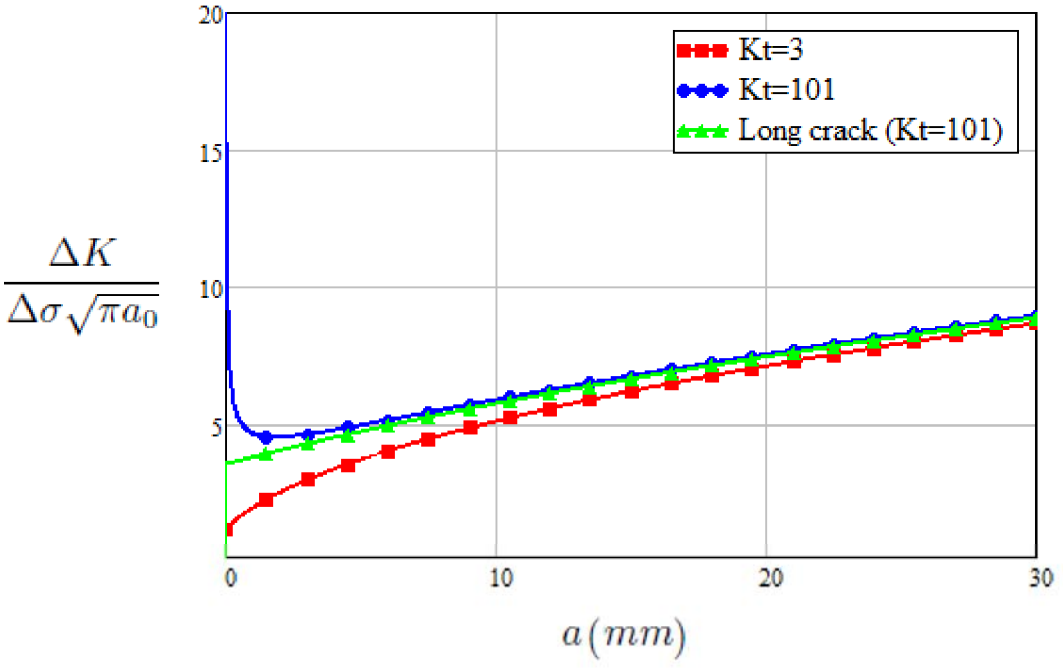

Figure 2.7: Non-dimensional ΔK vs. crack length

$$\Delta K_{th-short} = \eta\,\varphi(a)\Delta\sigma_{th}\sqrt{\pi(a+a_0)} \tag{2.28}$$

$$\Delta K_{th-long} = \Delta K_{th-short}(1+\frac{a_0}{a})^{-1/2} \tag{2.29}$$

Therefore, the threshold stress range that guarantees infinite fatigue life to the structural component is given by equation 2.32.

$$\eta\,\varphi(a)\Delta\sigma \quad \overline{\pi a} <= \Delta K_{th-long} \tag{2.30}$$

$$\eta\,\varphi(a)\Delta\sigma \quad \overline{\pi a} <= \Delta K_{th-short}(1+\frac{a_0}{a})^{-1/2} \tag{2.31}$$

$$\Delta\sigma <= \frac{\Delta K_{th-short}}{(1+\frac{a_0}{a})^{1/2}\eta\,\varphi(a) \quad \overline{\pi a}} \tag{2.32}$$

Using the stress intensity factor threshold defined by 2.29 and considering $\Delta\sigma = 50MPa$ for the two notches analyzed in figure 2.7 , the stress intensity factor by crack length is plotted in figure 2.8.

As per figure 2.8, both notches present infinite fatigue life for the stress range considered, however, the elliptical notch initiate a crack that stops to propagate with approximately 0.23mm length and can withstand a short crack with a length until 3.74mm, whereas the circular notch do not initiate any crack and allow short crack with length until approximately 8.1mm.

This figure is a good example for the decrease and increases behavior of stress

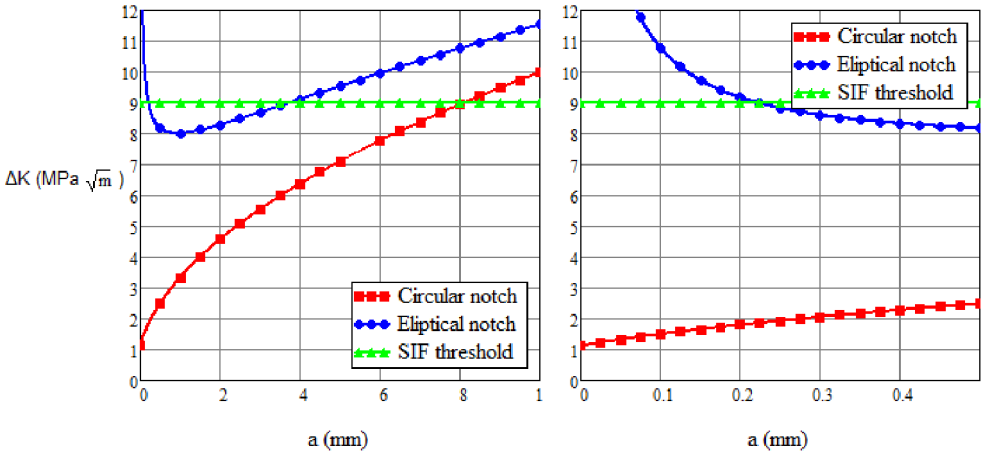

Figure 2.8: ΔK vs. a

intensity factor of cracks at sharp notches which allows the non-propagation crack phenomena.

The maximum tolerable stress range defined in equation 2.32 can be rewritten using dimensionless function as shown in equation 2.33 below as mention in reference [11].

$$\varphi(a/\rho) > \frac{(\Delta K_{th}/\Delta\sigma_l \quad \overline{\rho}).(\Delta\sigma_l/\Delta\sigma)}{((\eta\sqrt{\pi a/\rho})^2 + (\Delta K_{th}.\eta/\Delta\sigma_l \quad \overline{\rho})^2)^{1/2}} \tag{2.33}$$

Appointing the non-dimensional expression at right side of equation 2.33 above as a function g, the non-propagating crack criteria is satisfied when $\varphi/g < 1$ as presented in figure 2.9.

Figure 2.9 presents the ratio of the stress gradient and the dimensionless function g defined in the equation as a function of a/ρ for a crack from an elliptical notch with semi-axis equal to 10mm and 1mm, which correspond to $k_t = 21$, and $\Delta K_{th} = 9MPa \quad \overline{m}$ e $\Delta\sigma_l = 200MPa$.

Each curve corresponds to a different applied stress range defined as a non-dimensional function $\Delta\sigma_l/\Delta\sigma$.

The curve corresponding to $\Delta\sigma_l/\Delta\sigma = 4$ is tangent to the line $\varphi/g = 1.0$, which means that the maximum ratio $\Delta\sigma_l/\Delta\sigma$ that allows non-propagation cracks is approximately 4, then $50MPa$ is the maximum stress range that allows non-propagation cracks for this case.

The line corresponding to $\Delta\sigma_l/\Delta\sigma = 3$ is above the $\varphi/g = 1.0$ curve for all a/ρ ratios, which means that crack initiates and propagate at this stress range. Moreover, the line corresponding to $\Delta\sigma_l/\Delta\sigma = 21$, is all below the curve $\varphi/g = 1.0$ means that for stress ranges small than $9.5MPa$ no crack is initiated from the elliptical hole. In this case, the stress range at notch root is equal to the fatigue

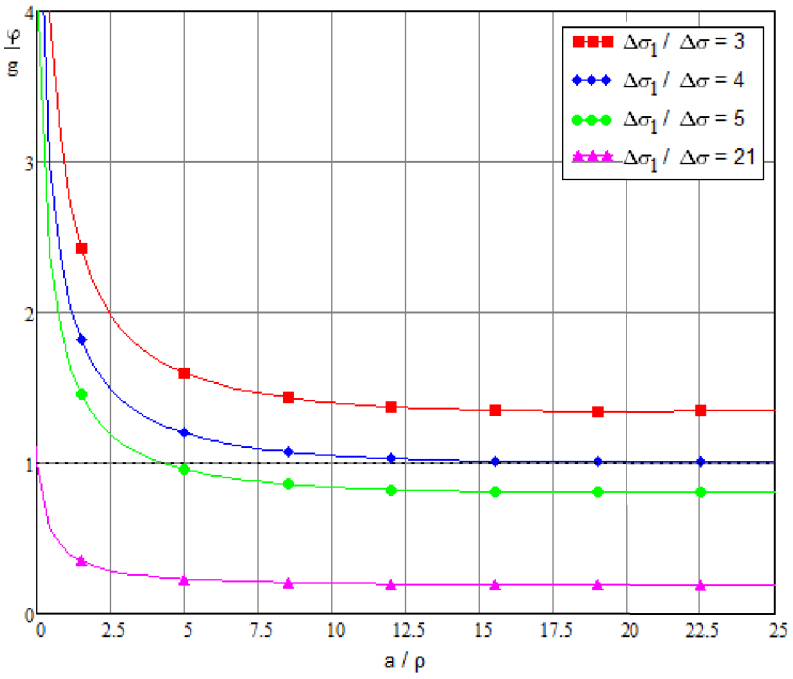

Figure 2.9: φ / g vs. a/ ρ

limit, since $\Delta\sigma_l/\Delta\sigma = k_t = 21$.

The line with $\Delta\sigma_l/\Delta\sigma = 5$ is an intermediate case where a crack initiate at notch root but become a non-propagating crack when the length reaches $a = 0.43mm$.

2.4 Short Crack at Elastic Plastic Regime

The non-propagating crack model in the elastic-plastic regime is studied through the short fatigue crack at notches using J-integral proposed by El-Haddad *et al.* [17].

In accordance with this model, the results based on the solution for J-integral shows that data for small crack length indicate higher crack growth rates than those predicted by the long crack model. Then, to avoid this discrepancy between short and long crack results, solution by J-integral can be modified to include the term a_0, the same defined in equation 2.22, to account for the behavior of short fatigue cracks in addition to plasticity correlation.

In this model, the same idea of the stress intensity factor at notches detailed in section 2.3, that uses an effective crack length as per equation 2.34 is considered.

$$a_{effective} = a + a_0 \tag{2.34}$$

And the additional crack length a_0 is the same considered in the elastic theory, represented by equation 2.35.

$$a_0 = \frac{1}{\pi}\left(\frac{\Delta K_{th}}{\Delta \sigma_l}\right)^2 \tag{2.35}$$

However, the non-propagating crack in the elastic-plastic regime proposed at reference [17] considers the J-integral approximation solution for plane stress crack problems at the exponential hardening plastic case discussed by reference [24]. This J-integral approximation is presented in equation 2.36.

$$\Delta J_{short} = 2\pi F^2 f(n)(a+a_0)(W_e+W_p) \tag{2.36}$$

Where,

F is a geometric dependent constant;

f(n) is a material constant related to the material hardening;

W_e and W_p are the elastic and plastic strain energy density respectively, as defined in section 2.2;

Although the model proposed in reference [17] considers plane stress condition, the idea can be expanded to the plane strain condition considering the approximation solution proposed also by Hutchinson at reference [23]. In accordance with section 2.2, the simple formulation between J and applied load for plane strain condition are presented in equation 2.37.

$$J_{long} = \alpha \sigma_0 \varepsilon_0 a (\sigma/\sigma_0)^{n+1} \hat{J}(a/b,n) \tag{2.37}$$

Considering the short crack behavior, J is as presented in equation 2.38.

$$J_{short} = \alpha \sigma_0 \varepsilon_0 (a+a_0)(\sigma/\sigma_0)^{n+1} \hat{J}(a/b,n) \tag{2.38}$$

Therefore, similar to the comparison of the stress intensity factor for short and long crack presented at equation 2.29, the J-integral considering the short crack model can be compared to the long crack J-integral model .

Thus, the relation between the J_{short} and the J_{long} are represented by equation 2.39.

$$J_{short} = (1+a_0/a)J_{long} \tag{2.39}$$

The crack will propagate when J-integral is higher than a threshold J-integral (J_{th}), which is a material property that can be measured following the ASTM E1820 code [25]. Therefore, the non-propagating crack only can be generated in the sharp notches where the J-integral, considering the short model, first decrease to a minimum value and then increase with the crack length a, the same way as for the stress intensity factor at linear elastic model presented in section 2.3.

Figure 2.10 presents a J_{short} from a notch with $\rho = 1mm$, blue line, that stop at a crack with $a = 1.8mm$ length, when J become small than the J threshold (J_{th}) presented by the dotted red line.

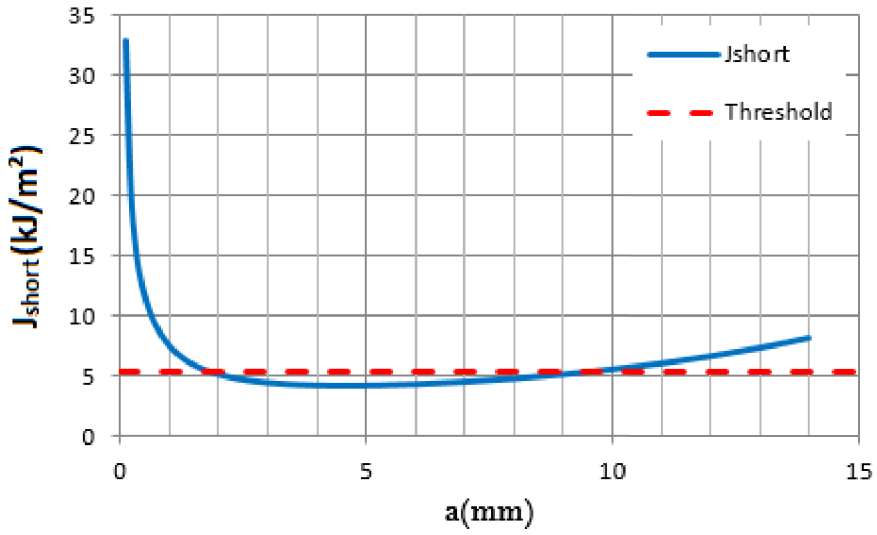

Figure 2.10: J_{short} vs. a and J_{th}

2.5 Stress Corrosion Cracking

Corrosion is defined as the destruction or deterioration of a material because of reaction with its environment and environment assisted cracking (EAC) is the general nomenclature for the cracking induced by the corrosive environment.

There are many categories of environment assisted cracking (EAC), among others, there is the stress corrosion cracking (SCC) which is defined as the cracking caused by the simultaneous presence of tensile stress and a specific corrosive medium.

Not all metal-environment combinations are susceptible to SCC. The SCC susceptibility is affected by the chemical composition of the metal and environment, grain orientation, distribution and composition of precipitates, dislocation interactions and more. The most common SCC susceptible environments are

the aqueous solutions, the liquid metals, fused salts and non-aqueous inorganic liquids [3].

Although the mechanism involved in the SCC are not well understood, and there is no specific mechanism that can be applied to all metals-environments systems which make its understanding more complicated [3],numerous SCC mechanisms have been proposed [2] [26]. However, there are two main mechanisms in the literature that describe the SCC, the dissolution mechanism, where and anodic dissolution occurs at the crack tip propagating the crack, and the mechanical model, which defend the idea that specific species adsorb and interact with crack tip strained metal bonds reducing the bond strength.

The appearance of SCC is fine cracks progressing through a material. There are intergranular SCC where the crack proceeds along the grain boundaries and transgranular cracking where crack do not have apparent preference path. Moreover, the SCC cracks can vary from single cracks to extreme branching cracks.

As suggested by the name, the stress is a very important parameter in the SCC phenomena. The stress can be from external loads, residual stresses or can be generated by corrosion products in constricted regions as an example. In a SCC, the crack can propagate under constant stress and increase stress should decrease the time before cracking since the SCC phenomena consist in a crack nucleation and after a crack propagation with a rate dependent on the stress applied. Moreover, it is usually accepted that there is an effective minimum or threshold stress at below it the SCC do not occur, since there are some standards that specify acceptable experimental practices to properly measure these properties as the ASTM F1624 [5] for the steel and hydrogen pair.

Even though the aim of this work is to consider the behavior of the stress corrosion cracks disregarding the corrosion mechanisms, the following sections briefly describe the mechanisms considered to validate this methodology.

2.5.1 Corrosion at hydrogen sulphide environment

As described in section 4-4, one of the experimental methodologies carried out in this work consider the AISI 4140 steel at H_2S aqueous environment in accordance with NACE TM0177[27] which is the code for experiments of stress corrosion cracking of metals in H_2S environments also called as sulfide stress cracking (SSC).

Since H_2S is an acid gas, when it is dissolved in aqueous environment it dissociates as presented by the reactions below.

$H_2S_{(aq)} \rightleftharpoons HS^- + H^+$

$$HS^{-} \rightleftharpoons S^{-2} + H^{+}$$

The ions H^{+} produced by H_2S dissociation on the surface of the metal produce a cathodic reaction that will initiate the anodic reaction on the metal leading to an electrochemical corrosion process in accordance with the following reactions:

Anodic reaction:

$$Fe - \quad Fe^{2+} + 2e-$$

Cathodic reaction:

$$2H^{+} + 2e- - \quad H_{2(g)}$$
$$2H^{+} + 2e- - \quad H^{0}$$

Besides the metal loss provided by the electrochemical corrosion presented above, the hydrogen atoms (H^0) that can be formed in the cathodic reaction can cause hydrogen damage in the metal as hydrogen embrittlement and hydrogen blistering.

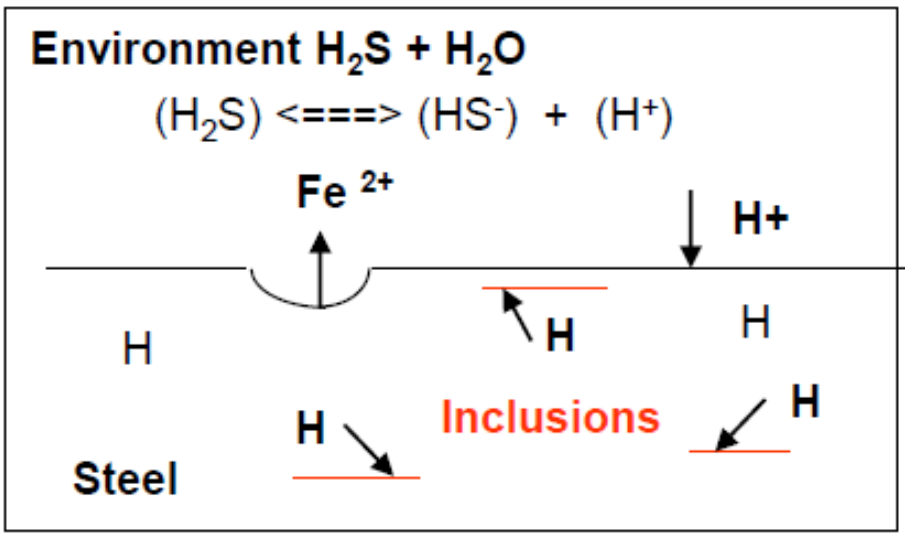

Figure 2.11: Hydrogen Embrittlement Mechanism.

The hydrogen embrittlement consists in the diffusion of the hydrogens atoms into the metal, these trapped hydrogen atoms will make the movement of the dislocations into the metal difficult and consequently blocking the plastic deformation making the material brittle. The main consequence of hydrogen embrittlement is the decreasing of the alloy toughness and the fracture resistance. Figure 2.11 shows the electrochemical corrosion at the surface of the metal and the hydrogen inclusions that cause the hydrogen embrittlement.

In addition to the hydrogen embrittlement, there is the hydrogen blistering, which is the damage also resultant of the absorption of hydrogen atoms. However, in the hydrogen blistering, these atoms combine to each other inside the metal to form hydrogen molecules (H_2) that cannot diffuse into the metal.

As the hydrogen gas within the void increases, the pressure increases causing rupture and cracking the material. The hydrogen blistering is schematically presented in figure 2.12.

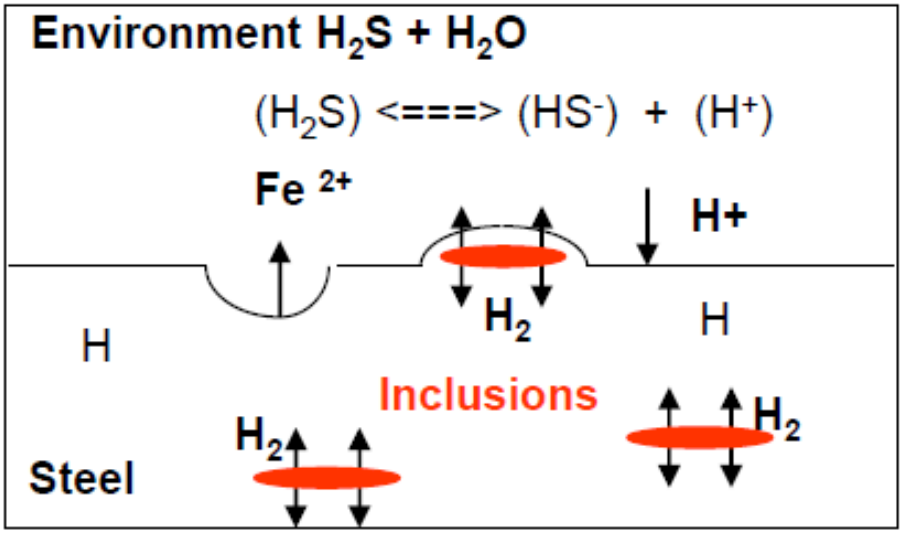

Figure 2.12: Hydrogen Blistering Mechanism.

Despite the simplistic explanation about the steel corrosion in hydrogen sulfide environment above, this corrosion process is well known due to its importance to the industry (i.e. chemicals, petroleum) and therefore there are standards to guide the experiments in this environment, making the confidence and repeatability of the results surest.

2.5.2 Liquid Metal Embrittlement Mechanisms

Unlike the steel in aqueous hydrogen sulfide environment discussed above, there is no standard for the liquid metal embrittlement of Aluminum in Gallium, which makes more difficult to guarantee the effectiveness and repeatability of the experiments, making the understanding of the corrosion mechanism more necessary.

Regarding the mechanism involved in the LME process, many authors use different mechanisms to explain the embrittlement caused by liquid metal and many references [28] [29] [30] [31] present a review between some available theories for the liquid metal embrittlement process.

The adsorption-induced reduction in cohesion mechanism is supported by Kamdar [28] and Benson & Hoagland [32]. In this theory, the embrittlement results from a liquid metal chemisorption-induced reduction in the strength of atomic bonds at the regions of stress concentrations in a solid metal, such as crack tips as presented on figure 2.13. As per this model, the crack propagation will occur when the stress acting in the solid atoms bond exceed the reduced breaking stress, and the liquid metal atom becomes stable chemisorbed on the freshly created surface, keeping the bond strength reduced. In this case, the crack growth can stop if the supply liquid metal is limited or interrupted.

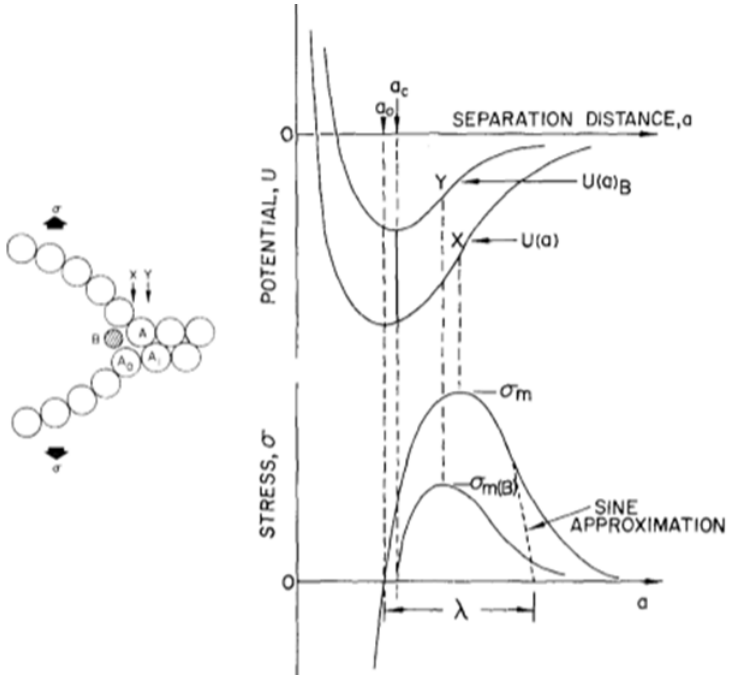

Figure 2.13: Schematic of adsorption-induced in cohesion mechanism.[28]

On the other hand, Fontana [3] and Vasudevan [33] support the stress assisted dissolution shown in figure 2.14, where dissolution occurs on freshly created surfaces, as crack tips, when the passive films are broken by local plastic deformation. In this theory, the crack propagates by the solution of the solid in the liquid under the influence of an applied stress, with volume diffusion of the dissolved solute through the liquid controlling the propagation.

Moreover, other theories to explain the LME mechanism as the reduction in surface energy, enhanced plasticity at the crack tip, intermetallic compound formation among others are mentioned in the literature.

Besides the mechanism that controls the liquid metal embrittlement process, the knowledge about the influence of the parameters in this process it is very important for the understanding of the experiments.

As mentioned above, the Liquid Metal Embrittlement (LME) is a very

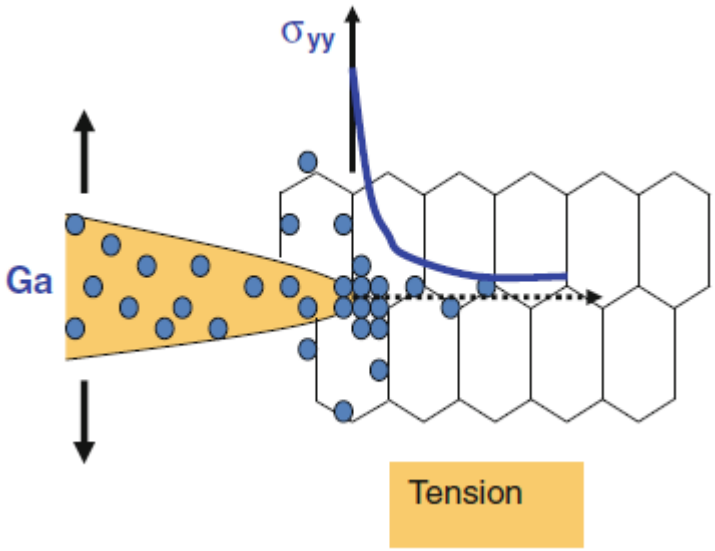

Figure 2.14: Schematic of Dissolution Mechanism.[33]

complex phenomenon, and researchers do not arrive at unifying principles governing the embrittlement process, there are important differences in the characteristics of LME that exist from one solid metal liquid metal system to another and different results from one author to another can be found in the literature.

However, some parameters have been appointed to have influence in the LME phenomenon as detailed below.

Since the grain boundaries are high energy areas and are more active chemically, the grain size, the grain boundary energy, the grain direction are frequently mentioned as parameters that influence the LME process. The liquid metal penetration into the grain boundary is proposed to explain the induced embrittlement, in special for the Aluminum-Gallium pair [29] [34] [35]. Moreover, the grain boundaries are considered as an obstacle to plastic flow and therefore potential sites of stress concentration also influencing the LME process.

However, since monocrystals of ductile metals are known to fracture by cleavage in the liquid metal environment as presented in figure 2.15, some authors as Kamdar [28] argue that the presence of grain boundary is not prerequisite for the occurrence of liquid metal embrittlement.

Temperature is another parameter that is mentioned to influence the liquid metal embrittlement susceptibility since temperature generally has influence in the LME mechanisms proposed above. As an example, elevated temperatures can cause the crack tip to become blunted due to ductility increasing, can affect the dissolution at the tip in the liquid metal environment and can control the rate of diffusion of the liquid metal atoms to the propagating tip among other phenomena.

However, as stated by Vasudevan and Sadananda [30], considering the stress assisted dissolution mechanism, an increase in temperature should increase the

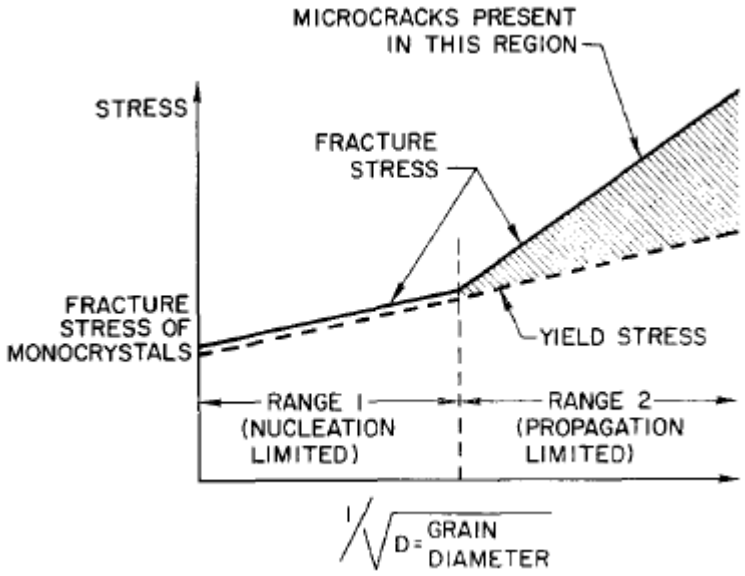

Figure 2.15: Effect of Grain Size on LME. [28]

diffusion rate and then increase the LME susceptibility, however, the embrittlement of liquid Hg in aluminum alloy presents and inverse relation with temperature, where the embrittlement in Hg is very rapid at room temperature in Al 2024 alloy while it is delayed at higher temperatures. Observations of LME susceptibility increasing with decreasing temperature was also noted by Kamdar [28] which defends that temperature has little effect on the susceptibility to embrittlement.

Moreover, observations that the severe embrittlement occurs near the freezing temperature of the liquid metal [28] [29] and observations of change in mechanism process at higher temperature [30] can be found in the literature.

In accordance with the general title of stress corrosion cracking, applied stress is usually identified as a prerequisite for LME. Usually, the alloy is negligible attacked in the no stressed condition, considering that a stress is required to create fresh new surfaces since the chemical force alone is not sufficient to create the cracked surface. However, the stress required is not necessary an external load applied since the presence of internal residual stress can induce a LME process [29].

A confusion idea is found in the literature regarding the requirement of stress for LME process, since embrittlement can occur without stress, by corrosion or by diffusion-controlled intergranular penetration process, however in this case is defined as another phenomenon than LME, since in the LME little or no penetration of liquid metal into the solid metal has been observed in accordance with Kamdar [28]. For the specific Al-Ga pair, Vasudevan [33] states that Ga transport is not stress dependent and Joseph *et al.*[29] states that the embrittlement of aluminum by Gallium can occur without any stress, however for both cases, the phenomenon

considered is not the LME.

Therefore, it can be concluded that the liquid metal embrittlement process is not well understood, and many authors disagree about the mechanism and parameters that influence the process making the experiment with liquid metal embrittlement challenging.

2.6 Residual Stress

Residual stress is defined as the stress that remains in mechanical parts that are not subjected to any outside stress and it is the result of the metallurgical and mechanical history of the material. Therefore, as the part should satisfy the equilibrium condition the residual stress is self-equilibrating, that is, the sum of the residual stresses and the moment due to residual stresses into a part should be zero. Moreover, the maximum residual stress allowed in any part is the material yielding stress, since if the residual stress is higher it will induce plastic deformation changing the residual stress distribution. The most of the manufacturing process introduces residual stress.

Figure 2.16 presents the profile of residual stress induced due to nonhomogeneous plastic deformation during lamination.

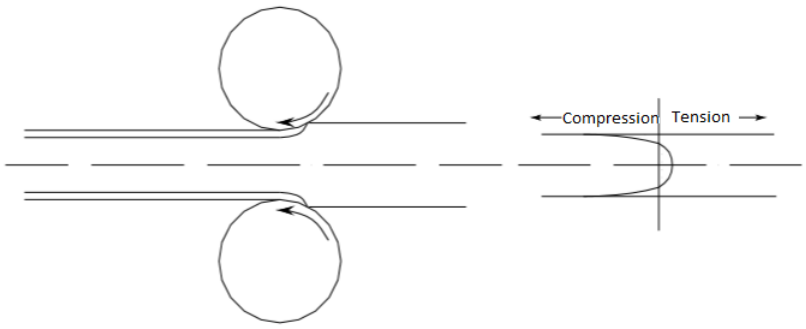

Figure 2.16: Residual Stress due to lamination. [37]

The residual stress can influence the material fatigue behavior, fracture strength, corrosion resistance, among others mechanical parameters. This influence can have a positive or negative effect, and because of this, the residual stress can be used to improve the mechanical behavior of the materials. Since the residual stress is an important parameter to predict the failure of a structure, there is an increasing interest in how the state of residual stress affects the mechanical properties of a material, the aerospace, automotive, and nuclear industries are already taken it into account in the advanced design [36].

There is some residual stress measurement techniques as the incremental hole drilling method, which is a destructive method that assesses the residual stress

evaluating its relaxation by measuring the strain or displacements after a layer removal. Other nondestructive methods for residual stress measurement are the x-ray and neutron diffraction. Both methods are based on measurement of lattice strains by studying variations in the lattice spacing of polycrystalline material. The x-ray diffraction is capable of measurement the residual stress on the surface of material whereas the neutron diffraction can measure the volume of the material. Moreover, the diffraction technique can assess all types of stress described in the next section [36].

In addition to the measurement techniques, some analytical and numerical models have been developed to predict the residual stress in a structure. Mechanical surface treatment models were developed for shot peening and cold rolling, while several finite element models were developed for welding, grinding heat treatment and thermal cutting. However, to obtain good results is necessary to do the three-dimensional calculations [36].

2.6.1 Types of residual Stress

Since the residual stress comes from a shape misfit, the residual stress field tends to scale with the extent of the misfitting region, therefore, they are commonly divided into three types by the length scales, Type I categorized as a macro stresses and Types II and III as micro stresses as per [38]. Figure 2.17 shows some sources of macro stresses and micro stresses.

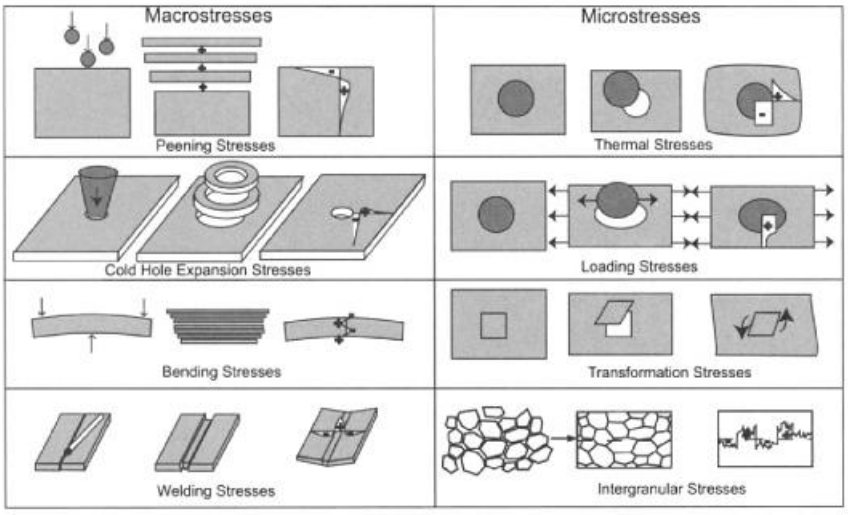

Figure 2.17: Macro stresses and micro stresses sources. [38]

Type I stresses self-equilibrate over a length which scales with the macroscopic dimension of the structure. They are assumed to be continuous from grain to grain, and indeed, even from phase to phase . Macroscopic plastic

deformation is a kind of source that generally generates residual stress type I as per figure 2.17

Type II stresses self-equilibrate over a length scale comparable to that of the grain structure. They are discontinuous from grain to grain. At least low-level of type II residual stress exist in polycrystalline materials because the thermal properties of differently oriented neighboring grains are different. Moreover, more type II stresses occur in multiphase materials because of large properties mismatches between phases.

Type III stresses self-equilibrate over a length scale smaller than the characteristic length scale of the microstructure. Their origin is misfits with a scale shorter than the grain scale as crystal defects.

Figure 2.18 presents schematically the types I, II and III of residual stress.

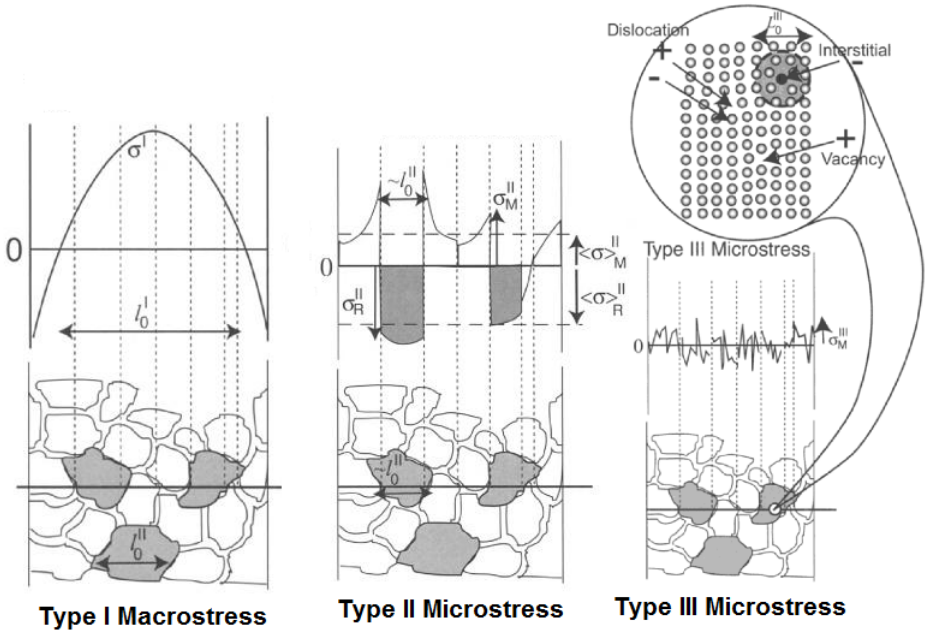

Figure 2.18: The three types of residual stress.

3
Methodology

3.1
Finite Element Method for Stress Intensity Factor at Linear Elastic Regime and J-integral at Elastic Plastic Regime

To predict the short crack behavior in a notched specimen, it is necessary to know how the stress decay in front of the notch, or how the stress intensity factor or the J-integral change as the crack growths from the notch in a linear elastic and elastic-plastic regime respectively.

In this section, the two-dimensional finite element analysis methodology used to estimate the stress intensity factor and J-integral in specimen geometry is described. The analyses were carried out using the commercial software *Abaqus/CAE*.

It is well known that there is an error associated with using two-dimensional analysis to determine the stress intensity factor and the J-integral in a three-dimensional specimen which is a function of the specimen thickness. However, the error is also presented in the measured fracture toughness threshold. As this methodology considers a comparison between calculated threshold and measured material thresholds, the two-dimensional analysis can be used for this purpose. In order that the calculated and measured fracture toughness have the equivalent error due to the two-dimensional methodology, the considered specimens have the same thickness.

The 8-node elements considered in the analyses are the standard quadratic quad elements with reduced integration, which in *Abaqus* environment corresponds to the CPE8R for the plane strain condition.

Sharp cracks are considered in these models, in *Abaqus* environment, a seam crack is defined in the internal edges that represent the crack. The seam geometry duplicates the nodes in the internal edge such that the elements on the opposite sides of the edge will not share nodes, and then the crack is allowed to open when tensioned.

The stress intensity factor (K_I) is calculated in *Abaqus* environment through the J-integral which is assessed through the virtual crack extension method proposed by Parks [39].

The *Abaqus/CAE* have specific tools for crack propagation analysis, however, the J-integral and the stress intensity factor can be assessed only in a static crack model. Because of that, a python code was developed to iteratively assess for the same geometry the J-integral for different crack sizes, and then extract automatically the $K_I xa$ and Jxa curves for a given geometry [40]. The python codes are presented at appendix A and B.

In the python code, the five J-integral contours are assessed, but the first J-integral contour is disregarded [41]. Therefore, the stress intensity factor and J-integral considered are the average for the second, third, fourth and fifth calculated values. The crack size by averages K_I and J are saved in a .txt file to facilitate the data handling.

3.1.1 Material Modelling

In the linear elastic regime, the material is modeled as linear elastic, where the stress is proportional to the strain by the Young's Modulus as per equation 3.1.

$$\sigma = E\varepsilon \tag{3.1}$$

In the elastic plastic regime, as stated on section 2.2, for the path independent J-integral assessment , the material shall be considered as the deformation plasticity model, which is a non-linear elastic behavior represented in *Abaqus/CAE* by the stress x strain relationship described in equation 3.2.

$$E\varepsilon = \sigma + \alpha \left(\frac{\sigma}{\sigma_0} \right)^{n-1} \sigma \tag{3.2}$$

The deformation plasticity model should be used with care to evaluate the J-integral since the material is modeled as non-linear elastic without unloading behavior and then energy dissipated due to plastic deformation is not taken into account.

However, in accordance with Simha *et al.* [42] the J-integral considering deformation plasticity material model at plane strain condition with uniform mesh with $0.5mm$ of element size present good results when the applied load does not start the remote plasticity at the back-face of the CT specimen.

3.1.2 Crack Tip

In linear elastic fracture mechanics, the stress and strains have the $1/\sqrt{r}$ singularity in the vicinity of crack tip and the elastic-plastic stress and strain field have the $1/r$ singularity, where r is the radial distance at the crack tip as shown in section 2.2.

Barsoum [43] demonstrates that the crack tip singularity can be reached using triangular 8-node quarter-point elements as the crack tip elements. Imposing the collapse nodes at crack tip constraint, the deformation field present a $1/\sqrt{r}$ singularity characteristic of linear elastic fields, whereas if the crack tip nodes are left free to displace independent of each other the $1/r$ singularity is obtained, which is the characteristic of perfect plasticity and blunting of the crack tip is obtained during the load.

These constraints can be obtained in *Abaqus/CAE* applying the collapsed element side singularity with a single node for the linear elastic case and duplicate nodes for elastic-plastic models as per figure 3.1.

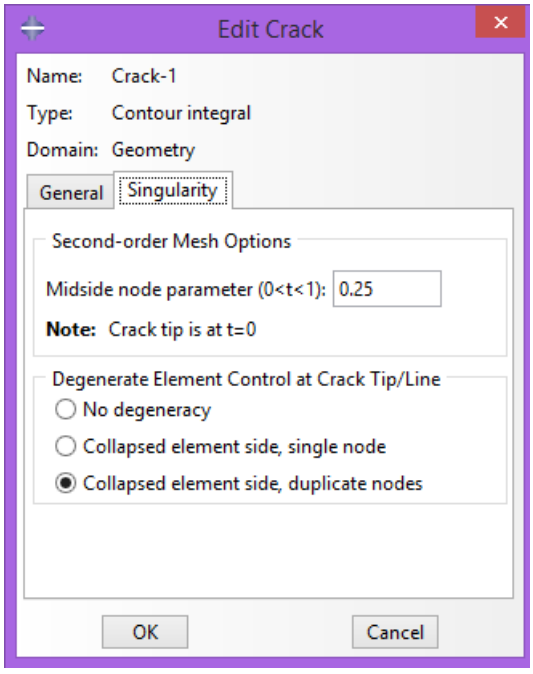

Figure 3.1: Abaqus windows for crack tip singularity definition

Moreover, the mid-side nodes of the elements at crack tip are moved to the quarter position as presented in figure 3.2 [44].

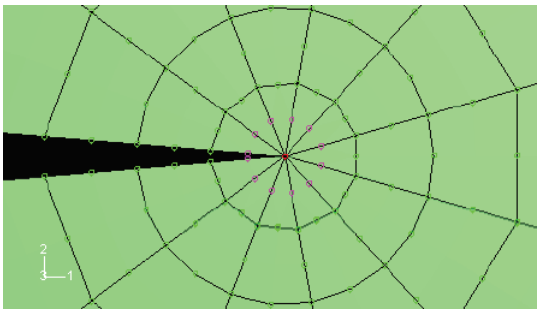

Figure 3.2: Crack tip mesh with quarter point elements

3.1.3 Boundary Conditions

A model for the ASTM standard Compact Specimen (CT) [25] were carried out to define the boundary condition and mesh configuration that best approximates the FEA results with the analytical equations presented in the code.

The dimensions and boundary condition considered for the CT ($W = 50mm, B = 25mm$) specimen are presented in figure 3.3.

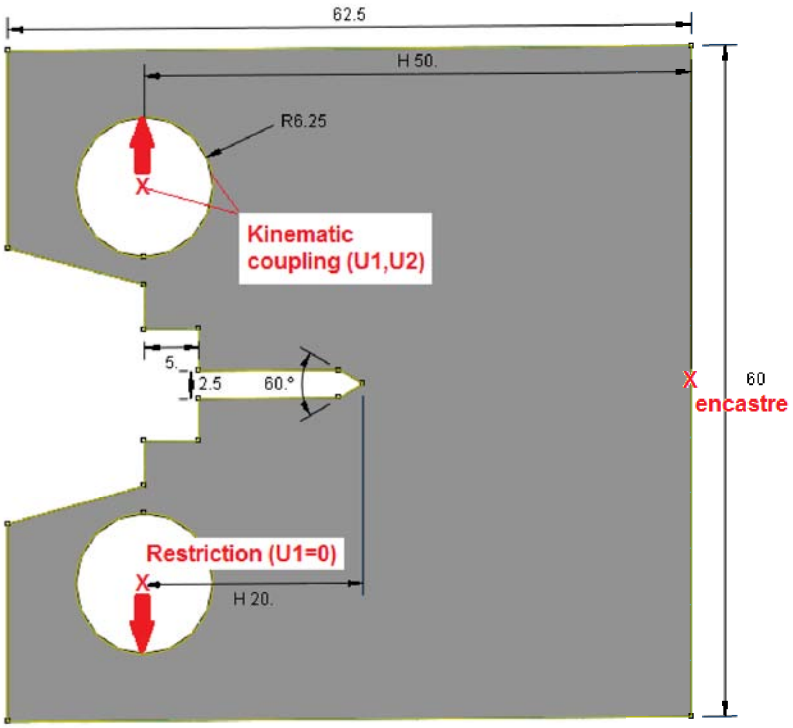

Figure 3.3: Standard Compact Specimen dimensions and boundary conditions (dimensions in mm)

As per figure 3.3, the compact specimen is restrained in one point of the geometry to avoid the rigid body movement, and the load is applied in the pin holes using a kinematic coupling constraint between the pin hole boundary and the center

of the hole. Moreover, a restraint in the movement in U1 for the pin hole center is added to simulate the alignment with the grab axis.

Other boundary conditions are analyzed, but, they are not representing significant change in the stress head of specimen notch.

3.1.4 Mesh

A mesh refinement was studied as per figure 3.4 in the linear elastic regime, in a CT specimen without a crack, where the stress ahead of the compact specimen notch is plotted against the distance from the notch for different mesh refinement. This study considers the entire model, and submodels to have a more refined mesh with less time of processing. *Submodel1* differs from *submodel2* in the size of the standard specimen considered as a submodel.

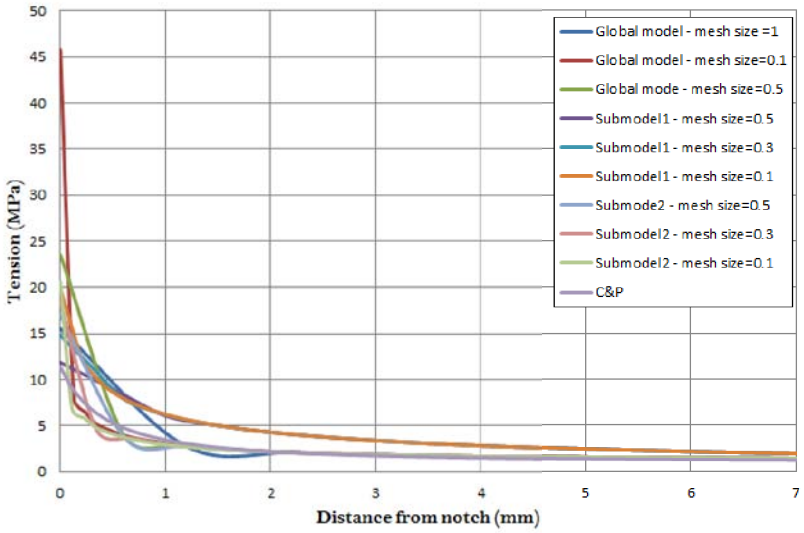

Figure 3.4: Stress ahead the notch in the standard compact specimen for different mesh refinements

As per figure 3.4, the stress ahead the specimen notch is very sensitive to the mesh refinement close to the notch, for this case until 2*mm* ahead the notch the models tested give very different stress profiles for the same specimen geometry and the same load applied.

However, as the stress decay ahead the notch is the responsible for the short non-propagating crack existence, it is not robust to assess the short crack behavior based on the stress profile, and then, the stress intensity factor and the J-integral will be the parameter considered in this work to predict the short crack behavior at linear elastic and elastic-plastic regime respectively.

The J-integral can be obtained with surprisingly coarse meshes in the linear elastic analysis, even though the local stress and strain are not very accurate whereas the stress field around a notch is very sensitive to the mesh refinement.

Moreover, for the elastic plastic modeling, a better mesh refinement is necessary for the crack tip for the J-integral evaluation.

Figure 3.5 shows the mesh proposed for the standard compact specimen (CT) model in linear elastic analysis with $0.5mm$ of element size whereas figure 3.6 shows the mesh proposed for the standard disc compact specimen (DCT) model in deformation plasticity material modeling, with also $0.5mm$ of element size and a mesh refinement with $0.1mm$ of element size in the crack tip.

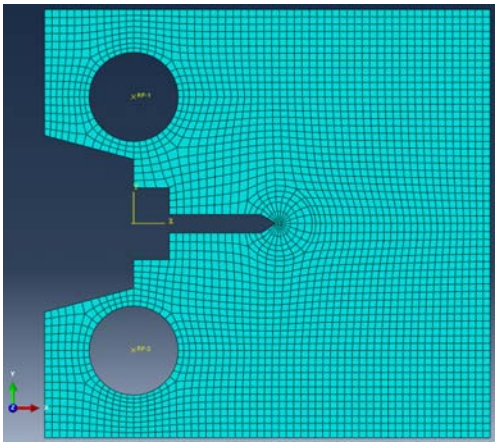

Figure 3.5: Standard compact specimen with a 0.5mm crack mesh

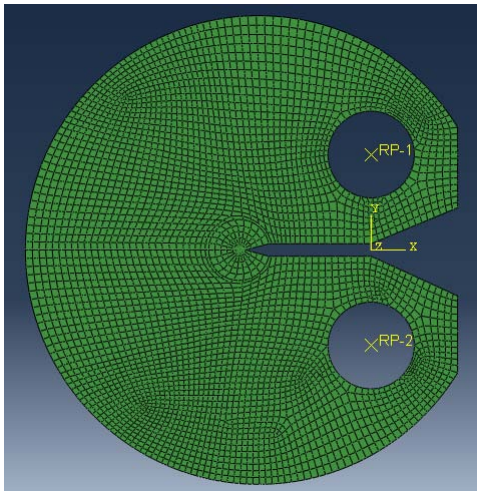

Figure 3.6: Standard disc compact specimen mesh

To guarantee the ring of quarter points triangular elements inserted along with concentric layers of structured quads, the geometry is partitioned by circular lines centered on the crack tip [44] and then quad-dominant sweep mesh control is assigned internally to the circular partitions. This configuration of mesh at crack tip widely used and is the same considered in the software *Quebra 2D* [45].

The stress intensity factor by the crack length at standard CT specimen $(W = 50mm, B = 25mm)$ under linear elastic regime is analyzed and compared to the analytical solution presented at ASTM 1820 ([25]).

The finite element model is carried out at each 0.1mm of crack length until 5mm and at each 1mm until 15mm of crack length. The results presented in figure 3.7 shows that the FEA considered is in accordance with the analytical model presented in the ASTM code, since the maximum error between the both models is 3%.

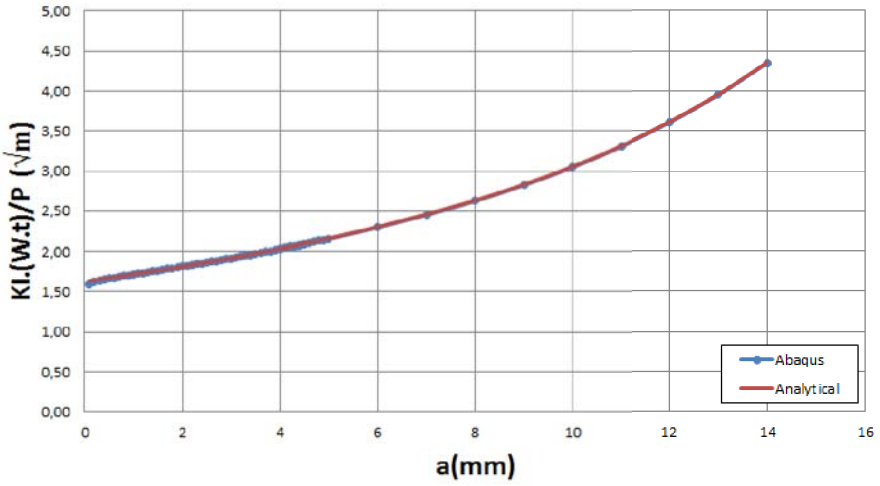

Figure 3.7: Stress intensity factor by crack length ahead of notch in standard CT specimen - analytical solution x Abaqus

Moreover, another verification of the FEA proposed is carried out in a CT specimen $(W = 50mm, B = 6mm)$ with a round notch $(b = 10mm, \rho = 1mm)$ as per figure 3.8 where the stress intensity factor by crack length ahead the notch from the FEA proposed is compared to the Quebra 2D software results [46].

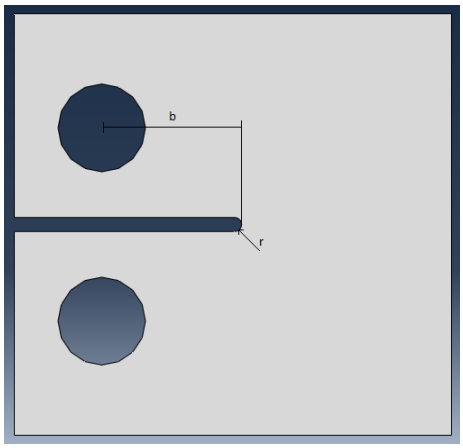

Figure 3.8: CT specimen with round notch

Both results are plotted in figure 3.9 shown again a good agreement between both methodologies and strengthening the methodology proposed in the present work.

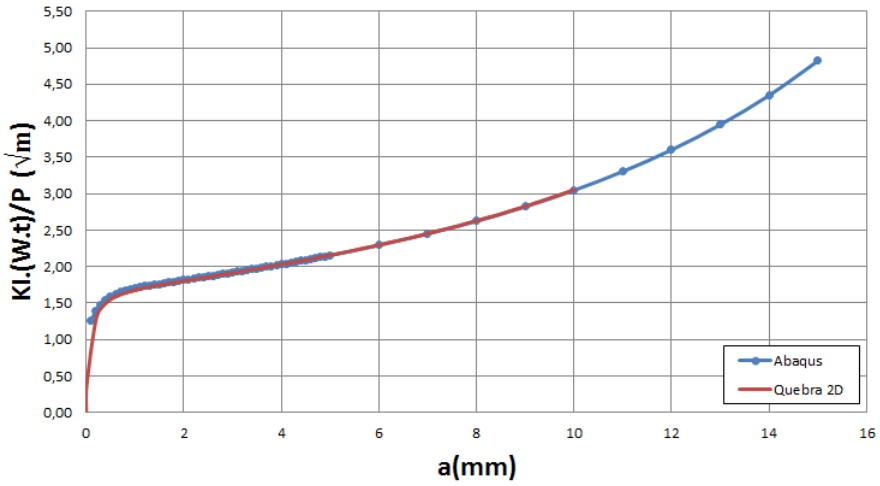

Figure 3.9: Stress intensity factor by crack length ahead of round notch in CT specimen - Quebra 2D x Abaqus

The same comparison was carried out considering the elastic-plastic regime. Figure 3.10 presents the J-integral evaluated using the finite element model and the ASTM 1820 [25] analytical formulation. As per this comparison, the FEA method gives results under 5% of error in comparison with the analytical methodology.

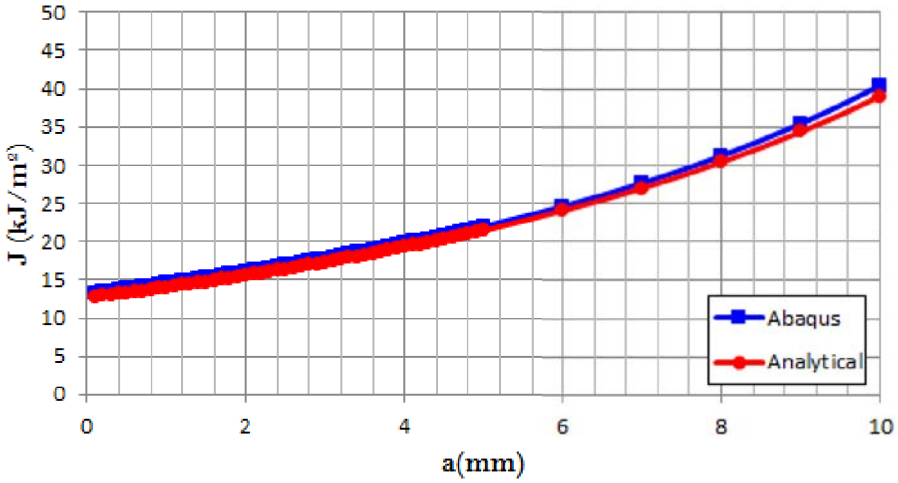

Figure 3.10: J-integral by crack length ahead of notch in standard DCT specimen - analytical solution x Abaqus

3.2 Residual Stress Induced by Plastic Deformation

A residual stress will be induced by plastic deformation in a four-point bent-beam specimen as per figure 3.11.

The four point bent-beam specimen was choose because its middle section is in pure bending, that is, there is no shearing stress and the bending moment induced is constant between the two middle supports, which allows more control of the actual stress acting in the specimen.

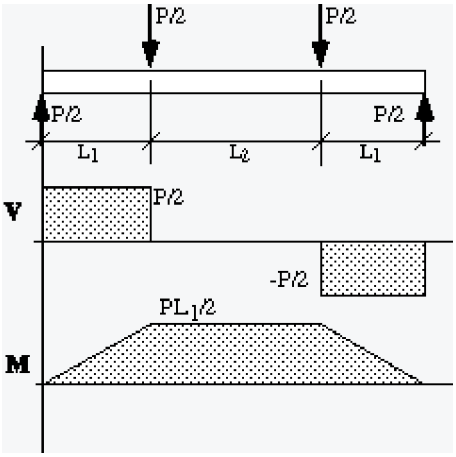

Figure 3.11: Shearing stress and bend moment in a four point bent-beam specimen. [47]

Therefore, the bent-beam specimen will be load reaching the plastic regime and then unload elastically. The residual stress will be the elastic-plastic subtracted by the elastic unload stress distribution.

To assess the stress distributions in the bent-beam cross section it will be considered that the cross section will remain flat after bending and the continuity of strain across the elastic-plastic boundary will be kept as recommended in [48]. Moreover, the transverse stress due to Poisson effects will be neglect.

Due to the continuity of strain, the strain distribution in the bent-beam specimen is linear and inversely proportional to the bent-beam radius ρ as per equation 3.3, where ρ and y are as per figure 3.12.

$$\varepsilon = \frac{y}{\rho} \tag{3.3}$$

A code in *Matlab* software is developed to calculate the stress distribution in the bent-beam specimen with rectangular cross section cited above. The code is presented in appendix C and is based on the Return-Mapping algorithms as per [49].

To calibrate the *Matlab* code, a simplified case considering the specimen as made of an elastic-perfectly plastic material with yielding stress equal to $\sigma_{y0} = 113,3MPa$ and Young Modulus equal to $E = 70GPa$ was carried out as per [14].

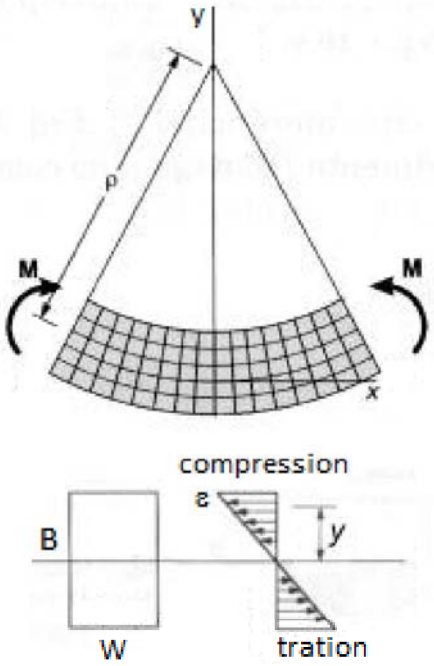

Figure 3.12: Strain distribution in bent-beam specimen

The stress-strain relation of an elastic-perfectly plastic material is presented in figure 3.13.

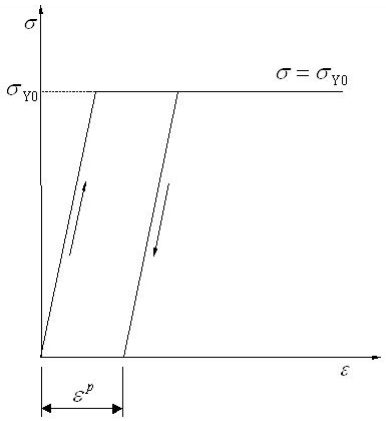

Figure 3.13: Stress x strain of an elastic perfectly plastic material

For a elastic perfectly plastic material, as per figure 3.13, the stress and strain are related by the Hook's law in the elastic regime and the stress is equal to the yielding stress in the plastic regime as per equation 3.4 where ε_E is the elastic limit deformation.

$$\begin{cases} \sigma = E\varepsilon, \varepsilon < \varepsilon_E \\ \sigma = \sigma_{y0}, \varepsilon > \varepsilon_E \end{cases} \tag{3.4}$$

In accordance with equation 3.3, the maximum strain and consequently the maximum stress will occur in the outer fiber of the cross section where $y = B/2$ as per figure 3.12. Based on this, the specimen will start the plastic regime when the outer fiber of the specimen cross section reaches the yielding stress.

Since in the elastic regime, the stress and strain are linear dependent as per equation 3.4, the stress can be described as a function of applied moment as per equations 3.5 to 3.8.

$$\sigma = \frac{My}{I} \tag{3.5}$$

$$I = \frac{WB^3}{12} \tag{3.6}$$

$$\sigma_{y0} = \frac{M_E.B/2}{WB^3/12} \tag{3.7}$$

$$M_E = \frac{\sigma_{y0} WB^2}{6} \tag{3.8}$$

And in accordance with figure 3.11, the applied moment is related to the applied force as per equations 3.9 and 3.10.

$$M_E = \frac{P_E L_1}{2} \tag{3.9}$$

$$P_E = \frac{\sigma_{y0} WB^2}{3L_1} \tag{3.10}$$

As the load increase, the subsequent fibers from cross section area will reach the yielding stress as per figure 3.14 until the middle of cross section reached also the yield stress and then the specimen reach the plastic collapse.

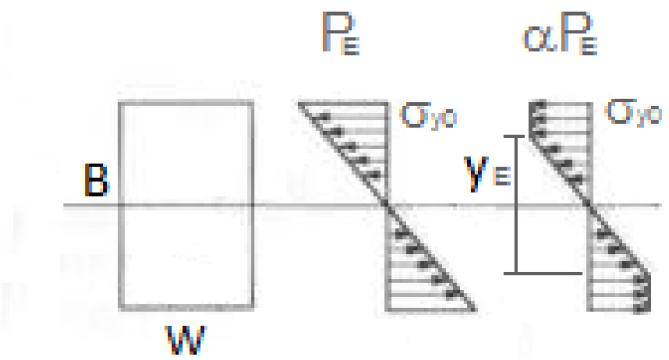

Figure 3.14: Stress distribution in the specimen cross section

As per moment equilibrium equation, when a load equivalent to αP_E is applied to the four-point bent-beam specimen:

$$M_{ext} = M_{int} \tag{3.11}$$

$$\frac{\alpha P_E L_1}{2} = \int_{-B/2}^{B/2} W\sigma(y)ydy \tag{3.12}$$

Due to the symmetry of cross section:

$$\frac{\alpha P_E L_1}{2} = 2W\int_{0}^{B/2} \sigma(y)ydy \tag{3.13}$$

For the elastic perfectly plastic case defined in equation 3.4:

$$\frac{\alpha P_E L_1}{2} = 2W(\int_{0}^{y_E/2} \frac{\sigma_{y0}y}{y_E/2}ydy + \int_{y_E/2}^{B/2} \sigma_{y0}ydx) \tag{3.14}$$

$$\alpha P_E L_1 = W\sigma_{y0}(\frac{B^2}{2} - \frac{y_E^2}{6}) \tag{3.15}$$

Replacing in equation 3.10, where y_E is the y distance of specimen that remains elastic as per figure 3.14.

$$\alpha L_1 \frac{\sigma_{y0}WB^2}{3L_1} = W\sigma_{y0}(\frac{B^2}{2} - \frac{y_E^2}{6}) \tag{3.16}$$

$$y_E = B \quad \overline{3-2\alpha} \tag{3.17}$$

In accordance with equation 3.17, the specimen will reach the plastic collapse when the $\alpha = 1,5$, in other words, when the applied force is $1,5P_E$.

Considering the continuity of strain , and by the similarity of triangles:

$$\frac{\varepsilon_{max}}{B/2} = \frac{\varepsilon_E}{y_E/2} \tag{3.18}$$

$$\varepsilon_E = \frac{\sigma_{y0}}{E} \tag{3.19}$$

$$\varepsilon_{max} = \frac{\sigma_{y0}}{E \quad \overline{3-2\alpha}} \tag{3.20}$$

Considering the cross section as rectangular with $B = 5mm$ height, $W = 15mm$ wide and the distance between the supports $L_1 = 25mm$, and the material as a elastic perfectly plastic with $\sigma_{y0} = 113.3MPa$ and $E = 70GPa$, we have after loading by $P_c = 679,8N$ which means $\alpha = 1,2$, the maximum strain will be $\varepsilon_{max} = 2,09.10^{-3}$ as per equation 3.20 and the maximum stress will be $\sigma_{max} = 113,3MPa$ for the simplified elastic perfectly plastic case defined above.

Figure 3.15 presents the strain distribution in the cross section and figure 3.16 is the stress distribution after loading by $P_c = 679,8N$.

To unload the specimen is equivalent to load with $P = -\alpha P_E$. As the unload is elastic, its obey the Hook's law defined in equation 3.4, and thus the strain and stress due to unloading are:

$$\varepsilon_d = -\frac{\alpha\sigma_{y0}}{E} \tag{3.21}$$

$$\sigma_d = -\alpha\sigma_{y0} \tag{3.22}$$

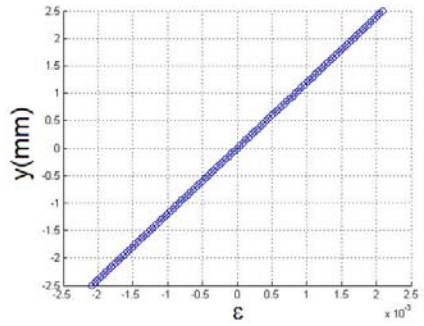

Figure 3.15: Strain distribution in the specimen cross section after loading

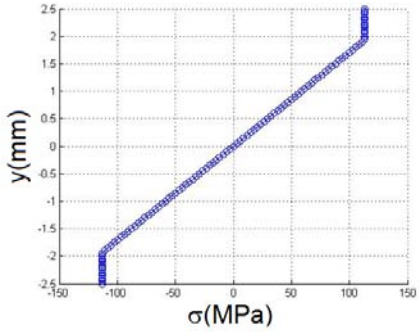

Figure 3.16: Stress distribution in the specimen cross section after loading

Considering the values defined above, the unloading stress in the outer fiber is $\sigma_d = -135,96MPa$ as per equation 3.22 whereas the unloading strain is $\varepsilon_d = -1,94.10^{-3}$ in accordance with equation 3.21.

Figure 3.17 presents the stress distribution due to unloading by $P_c = -679,8N$.

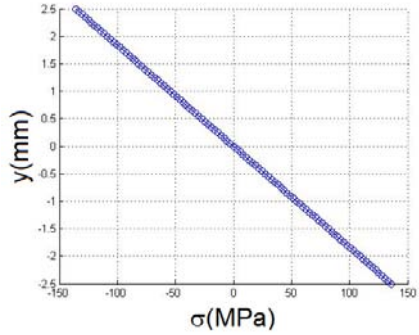

Figure 3.17: Stress distribution in the specimen cross section due to unloading

Since the residual stress will be the elastic-plastic subtracted by the elastic unload stress and strain distribution, in $y = B/2$:

$$\sigma_{res} = \sigma_{y0} - \alpha\sigma_{y0} \tag{3.23}$$

$$\varepsilon_{res} = \varepsilon_{max} - \frac{\alpha\sigma_{y0}}{E} \tag{3.24}$$

Thus, the residual stress is $\sigma_{res} = -22,66MPa$ as per equation 3.23 and the residual strain is $\varepsilon_{res} = 0,15.10^{-3}$ in accordance with equation 3.24.

Figures 3.18 and 3.19 present the residual stress and strain distribution respectively considering the values defined above.

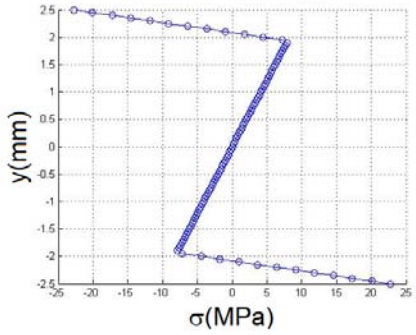

Figure 3.18: Stress distribution in the specimen cross section due to unloading

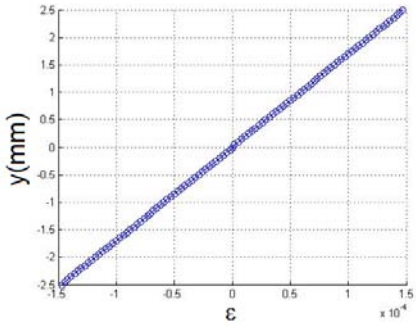

Figure 3.19: Stress distribution in the specimen cross section due to unloading

The stress-strain diagram for the load and unloading of the outer fiber of the specimen is presented in figure 3.20. As per this figure, the residual stress and residual strain can also be verified.

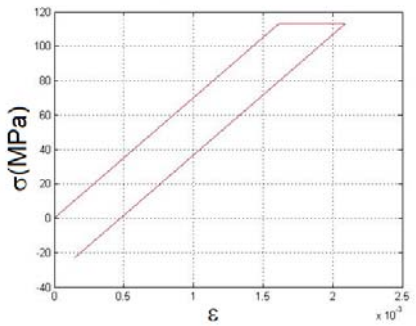

Figure 3.20: Stress x strain from load and unloading

4
Experimental Procedures

4.1
Stress Corrosion Cracking of Steel in hydrogen sulphide environment experiment procedure

The mathematical models proposed at section 3.1 were validated considering the stress corrosion cracking of AISI 4140 steel defined at section 4.1.1 in H_2S environment following the NACE TM0177 standard [27] which aims testing metals for resistance to cracking failure under the combined action of tensile stress and corrosion in an aqueous environment containing hydrogen sulfide (H_2S).

The Disc Compact Specimens (DCT) tested were made from an AISI 4140 steel round bar with the notches machined by electrochemical erosion to avoid residual stress in the notch. The specimens were grinding with SiC sandpaper P600 grade, degrease with acetone and dry with hot air following the ASTM G1 [50] specimen preparation procedure.

Figure 4.1 shows a prepared specimen.

Figure 4.1: Prepared DCT specimen

The specimen is loaded through a proof-ring device that was calibrated with a load cell before the test. The load in the proof-ring is controlled through strain gauges attached in the proof-ring.

A test solution B which consist of 5.0$wt\%$ $NaCl$, 0.4$wt\%$ sodium acetate (CH_3COONa), and 0.23$wt\%$ glacial acetic acid (CH_3COOH) dissolved in distilled water is prepared and stored beside the test vessels as per figure 4.3.

The prepared test specimens are assembled inside the test vessel connected to the proof-ring. The stressing fixtures inside of the test vessel are electrically isolated from the test specimen, the isolation was checked before the experiment with a multimeter. Moreover, the stressing fixtures are coated with Teflon tape as per figure 4.2.

Figure 4.2: The test vessel with the DCT specimen before the test

Leakage in the assembled system are verified and the system and the test solution are purged with inert gas (N_2) to ensure that the test solution is oxygen-free before introducing H_2S.

The test solution is transferred to the test vessel and then a gas mixture with $125mbar$ of H_2S and $875mbar$ of CO_2 are used to saturate the test solution and a continuous flow are kept during the test at a low flow rate to maintain the H_2S concentration and slight positive pressure to prevent air from entering the test vessel through small leaks. Figure 4.3 shows the test apparatus.

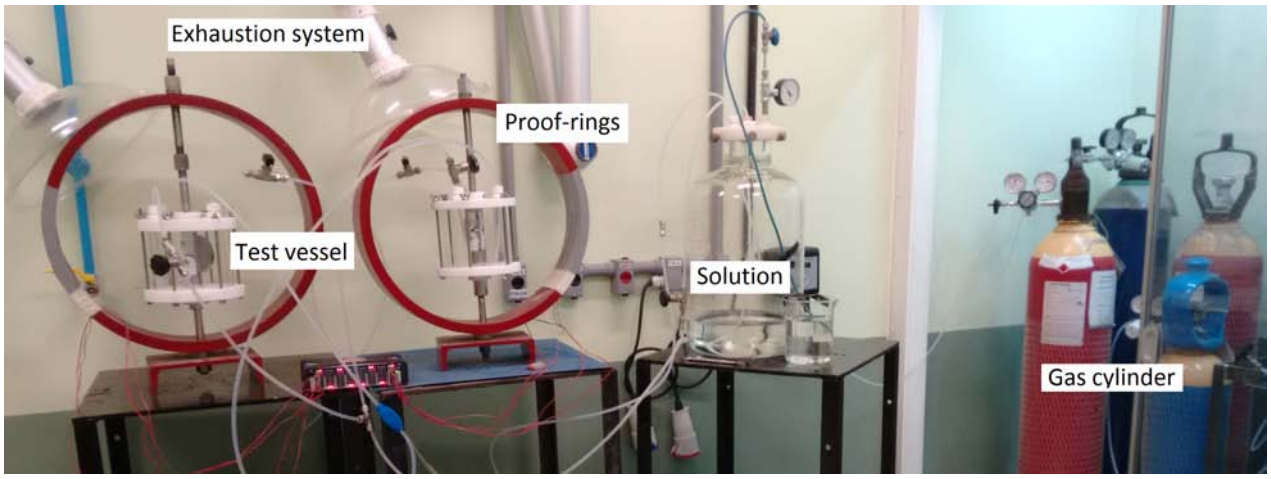

Figure 4.3: SCC in H_2S environment apparatus

The room temperature is kept during the entire test.

4.1.1 Steel AISI 4140 properties

The AISI/SAE 4140 is a heat-treatable low-alloy steel that combines moderate hardenability and good strength and toughness, and it is subjected to hydrogen embrittlement when subject to heat treat to high strength levels [51].

This steel has the following chemical composition: $0.38\% - 0.43\%$ of C, $0.75\% - 1.00\%$ of Mn, 0.030% of P, 0.040% of S, $0.15\% - 0.35\%$ of Si, $0.80\% - 1.10\%$ of Cr and $0.15\% - 0.25\%$ of Mo.

The SAE 41XX series steels contain Cr and Mo as key alloying elements. The Cr is used to impart oxidation and corrosion resistance, hardenability and high-temperature strength, whereas Mo is used to increase strength, control hardenability and reduce the tendency to temper embrittlement [52].

The mechanical properties of the AISI/SAE 4140 are a function of the heat treatment. For $50mm$ round bar quenched from $845\,^{\circ}C$ and tempered at $540\,^{\circ}C$, the tensile strength is $920MPa$ and yield strength is $750MPa$, whereas, for $75mm$ round bar with the same quench and tempering temperatures, the tensile strength is about $860MPa$ and the yield strength is $655MPa$.

Moreover, the stress x strain curve and tensile properties of the round bar used to machine the steel notched specimens is acquired in accordance with ASTM E8 standard [53] and are presented in figure 4.4.

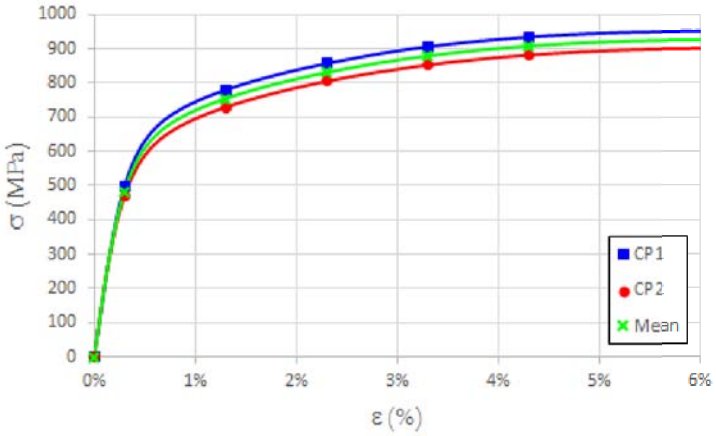

Figure 4.4: Stress x strain curve of AISI 4140

Based on the experimental curves, the elasticity modulus and the yield strength for the used AISI/SAE 4140 steel is $201324 \pm 2979MPa$ and 609 ± 40 MPa respectively.

Since the finite element model used to predict the behavior of the steel specimens consider the deformation plasticity material modeling from *Abaqus*, the stress x strain curve should be write as the equation 4.1.

$$E\varepsilon = \sigma + \alpha \left(\frac{\sigma}{\sigma_0} \right)^{(n-1)} \sigma \tag{4.1}$$

A regression analysis was carried out to find the equation 4.1 parameters that minimize the square root difference between the analytical curve and the experimental stress x strain curve.

Table 4.1: Stress x strain curve parameters definition

E	201324
σ_0	350.8
α	0.023
n	7

The both curves are presented in figure 4.5 and the calculated parameters are presented in table 4.1.

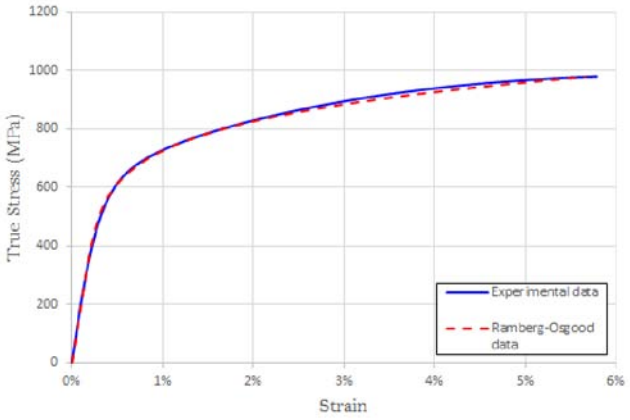

Figure 4.5: True stress x strain curve

Furthermore, the AISI 4140 steel properties under Sulphide Stress Cracking (SSC) conditions were carried out considering the solution B from NACE TM0177 standard [27] which is an aqueous solution containing $5wt\%$ sodium chloride $(NaCl)$, $2.5wt\%$ of glacial acetic acid (CH_3COOH) and $0.4wt\%$ of sodium acetate (CH_3COONa) with a pH in a range from $3.4-3.6$, saturated with $125mbar$ of H_2S and $875mbar$ of CO_2 at room temperature.

The crack initiation threshold (S_{SCC}) in this environment was prospected using small incremental load steps following ASTM F1624 standard [5] procedure, resulting in a threshold measurement equal to $S_{SCC} = 332MPa$.

Moreover, the cracking propagation threshold was measured in accordance with NACE TM0177 [27] method D standard, resulting in a $K_{SCC} = 34.2MPa.\ \overline{m}$.

The details of both measurements are presented in the reference [15].

Furthermore, the crack initiation threshold for the elastic-plastic regime (J_{SCC}) in the same environment was measured in accordance with ASTM E1820 [25] standard. Figure 4.6 shows the experiment apparatus.

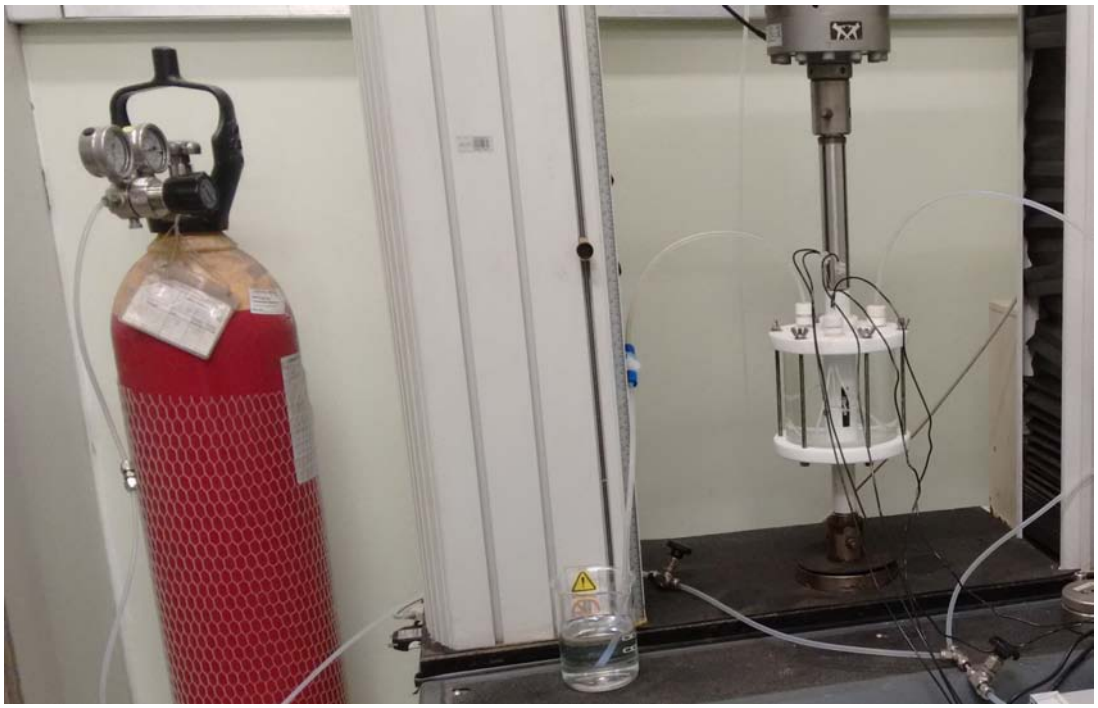

Figure 4.6: J_{SCC} experiment apparatus.

The J_{SCC} was measured using DCT specimens with $W = 32mm$ and $B = 8mm$ to keep the same thickness of the tested notched specimens.

In accordance with ASTM E1820 [25] methodology, J is calculated as a sum of an elastic and a plastic component as per equation 4.2.

$$J = J_{el} + J_{pl} \tag{4.2}$$

Where, the elastic component is a function of the stress intensity factor calculated based on the applied load following equation 2.16.

In this test, the specimen has a narrow notch with $14.5mm$ length that was fatigue pre-cracked to reach $16mm$ as initial crack size, and the specimen was loaded until the crack length reaches approximately $28mm$.

At the end of this test, the elastic part of the propagation threshold is $K_{SCC} = 34.1MPa$. $\overline{m}$, which is in accordance with the K_{SCC} measured as described above.

And finally, the J-integral threshold of the AISI 4140 steel in the considered environment is $J_{SCC} = 11.7kJ/m^2$.

4.2
Effect of Residual Stress on LME Experimental Procedure

The resistance to Liquid Metal Embrittlement (LME) of the four point bending specimens with well known residual stress imposed by plastic deformation following the model presented in section 3.2 was carried out in accordance with the procedure described in this section.

Since there is no standard procedure for the LME of Aluminum Gallium pair as there is for the SCC of steel in hydrogen sulfide environment presented in section 4.1, two different procedures were tested following the recommendation based on Gallium behavior described in section 2.5.

4.2.1
Specimens Preparation

The four-point bending specimens were flat strips with 15*mm* wide, 5*mm* thickness and 110*mm* length cut from an 0.5*in* Aluminum plate detailed in section 4.2.4. Figure 4.7 presents the Aluminum bending specimen.

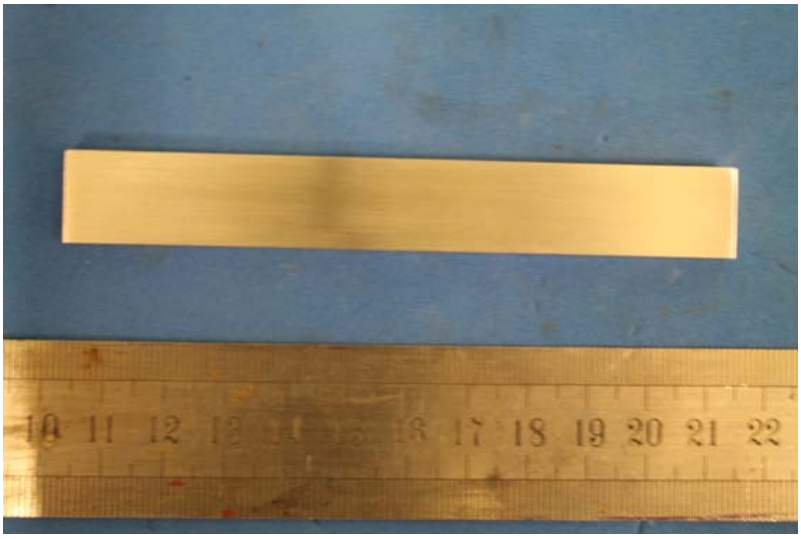

Figure 4.7: Four-point bending specimen

The specimens were grinding by SiC sandpaper grade P600 and cleaned submerged in Acetone and exposure to ultrasound by approximately 5*min* in accordance with ASTM G1 [50] procedure and shown in figures 4.8 and 4.9

The specimens dimensions, thickness, wide and length are measured using a caliper rule.

A residual stress was imposed using the four-point bending apparatus loading the specimens to reach a known plastic deformation following section 3.2 methodology as presented in figure 4.10.

Figure 4.8: Specimens cleaning using ultrasound

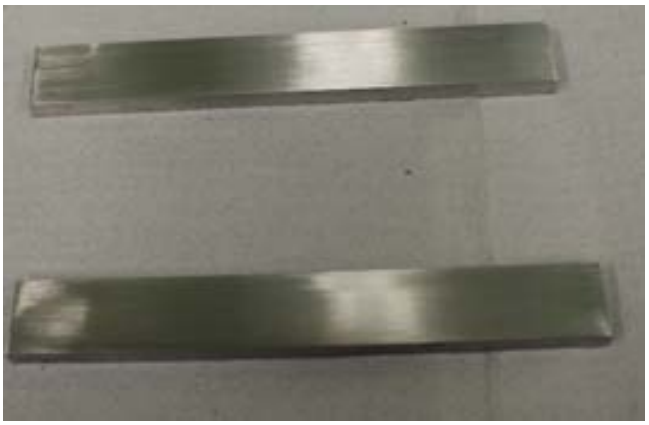

Figure 4.9: Four-point bending specimens cleaned

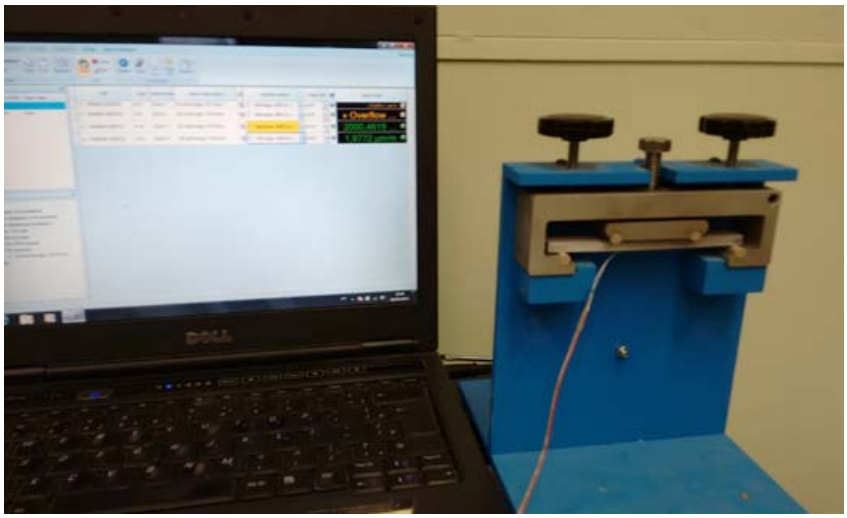

Figure 4.10: Apparatus used to impose plastic deformation that induce residual stress on the specimens

The plastic deformation was controlled by a strain gauge (*Kyowa* strain gauge with $2.09 \pm 1.0\%$ gauge factor and $120.0 \pm 0.8\Omega$ gauge resistance for use in Aluminum) attached to the middle of the specimen as shown in figure 4.11.

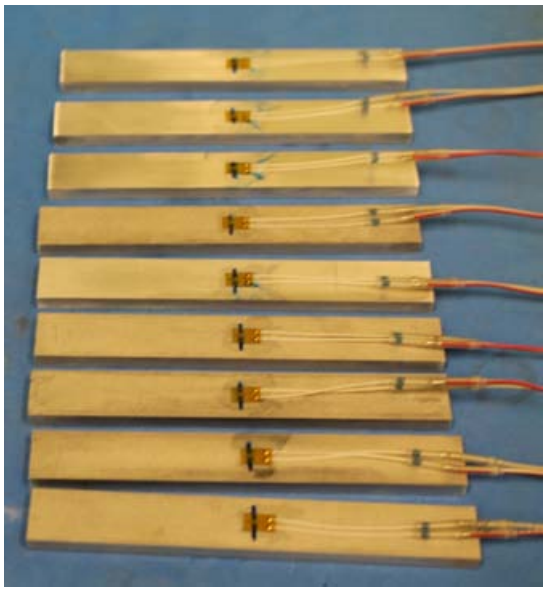

Figure 4.11: Strain gauge in the specimens to measure the imposed residual stress

After the residual stress be induced in the bending specimens, the specimens and the Gallium were heated to until approximately $35.0°C$ using a greenhouse or incandescent lamp. When the specimens reach the temperature, the Gallium was applied in the face of the specimen using a brush as per figure 4.12.

Figure 4.12: Gallium applied in the specimens

To guarantee the homogeneity of the metallurgy of the specimens, the Gallium will be applied in the face of the specimen that was cut from the middle of the plate for all the specimens.

4.2.2 Constant Displacement Procedure

The first procedure was based on ASTM G39 [54] standard.

All specimens are pre-loaded with $10.0MPa$. The stress was controlled by a dial indicating comparator device as per figure 4.13 since the strain gauge could not

be kept in the specimen after Gallium application because the Gallium dissolution or adsorption in the specimen surface do not allow to keep the strain gauge attached.

Figure 4.13: Dial indicating comparator to control the stress imposed in the specimens

The specimens were maintained inside a greenhouse at a constant temperature equal to $35.0°C$ as per figure 4.14 and every $24hours$ the load was increased in $5.0MPa$ using also the dial indicator comparator apparatus to control the load.

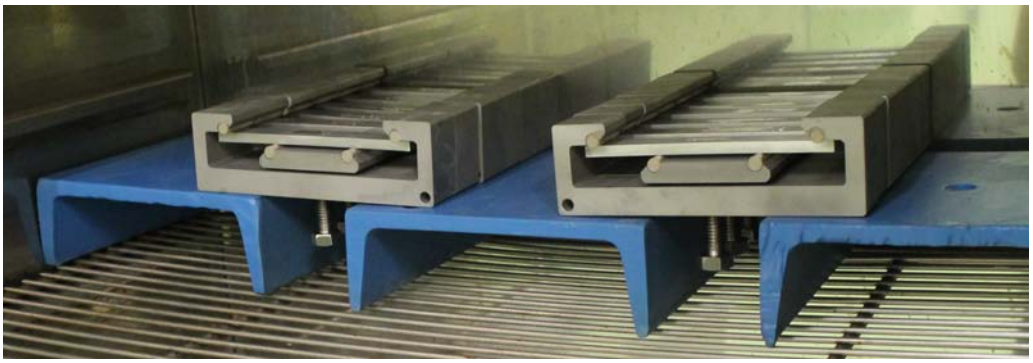

Figure 4.14: Specimens inside the greenhouse

There was no success in this experimental procedure since it was not possible to verify the load that initiates the crack by LME.

4.2.3 Slow Strain Rate Procedure

The second experimental procedure was carried out based on ASTM G129 [55] standard.

The four-point bending loading apparatus was fixed to an electromechanical machine (INSTRON model 5582) and an incandescent lamp of $60W$ was placed

close to the specimen to keep the experiment at approximately $35.0°C$ of temperature with the help of an aluminum paper covering the apparatus. The temperature was controlled using a thermocouple fixed close to the specimen.

Figure 4.15 shows the experiment apparatus.

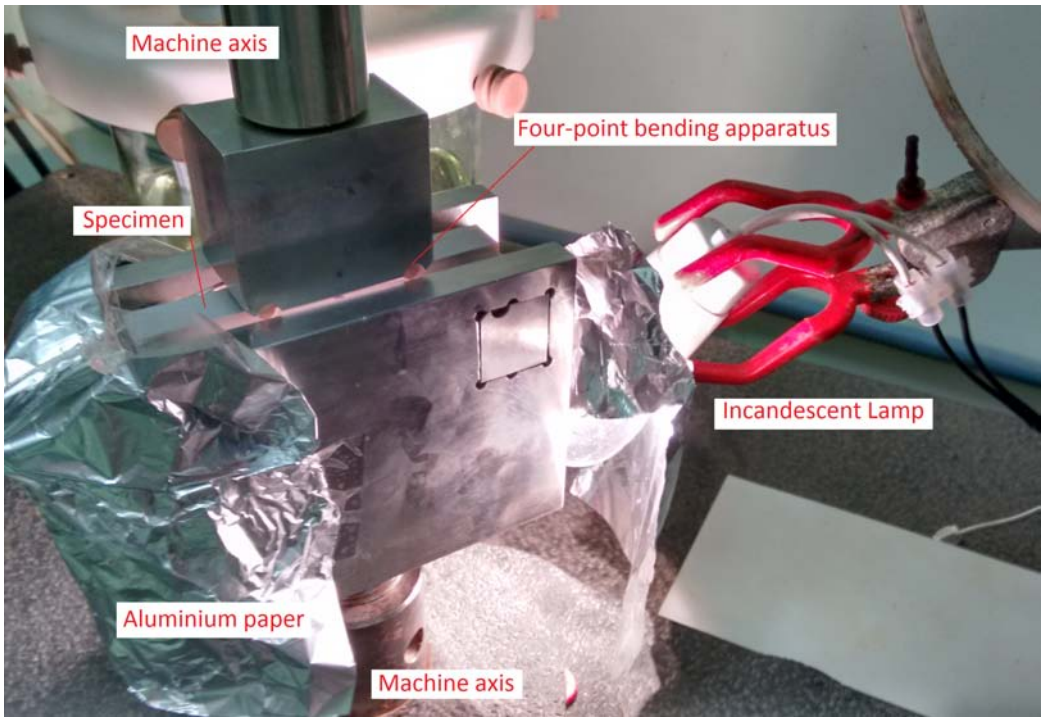

Figure 4.15: Slow Strain Rate apparatus

After reach a required temperature, a pre-load of approximately $200N$ was applied and after that, a constant displacement rate equal to $10^{-5}mm/s$ [56] [55] was performed in the four-point bending device.

The environmental assisted cracking resistance was then obtained when the specimen breaks and the load have a quickly decrease as presented in figure 4.16, which shows the load vs. displacement for the CP2 which breaks at $674N$.

4.2.4 Aluminum 2024 T351 properties

The Aluminum 2024 T351 alloy is commonly alloy used for aircraft structures. This material has a high strength-weight ratio and good fatigue resistance.

This Aluminum alloy have the following composition in accordance with ASM Handbook [51]: 0.50% of Si, 0.50% of Fe, $3.80\% - 4.90\%$ of Cu, $0.30\% - 0.90\%$ of Mn, $1.20\% - 1.80\%$ of Mg, 0.10% of Cr, 0.25% of Zn and 0.15% of Ti.

The typical mechanical properties of the Al 2024-T351 alloy is $E = 73GPa$, $470MPa$ of ultimate tensile stress and $325MPa$ of yield stress.

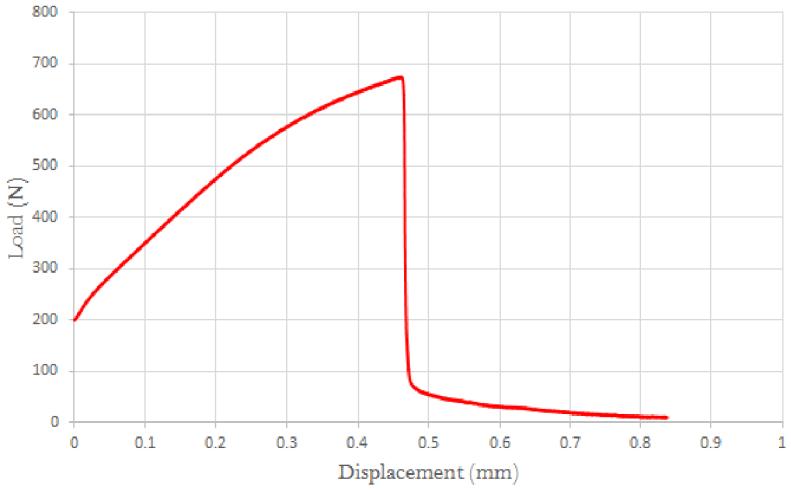

Figure 4.16: Load vs. Displacement of a slow strain rate experiment

The Aluminum plate was annealed before the specimen preparations to release the residual stress and cold work deformation due to the rolling process.

The annealing process was carried out in a metallurgical furnace following the ASM Handbook [51] procedure. The plate was heated until $415°C$ and this temperature is kept during 2h. After that the plate was cooling at a low rate (less than $28°C/h$).

After annealing, the stress vs. strain curve and tensile properties of the aluminum plate were measured following the ASTM E8 [53] procedure. The curves are presented in figure 4.17.

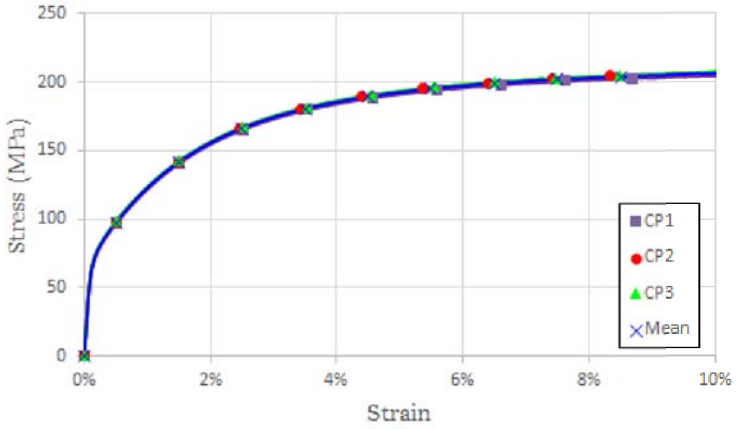

Figure 4.17: Stress x strain curve of Aluminum alloy

Since the residual stress model for the Aluminum specimens detailed in section 3.2 are based on the predictor-corrector code detailed in appendix C, the bilinear Ramberg-Osgood parameters represented in equation 4.3 is assessed using

Table 4.2: Ramberg-Osgood parameters

E	67426
σ_0	59.4
H_b	1226.8
h_b	0.61

a regression analysis to minimize the error between the experimental curve and the Ramberg-Osgood curve.

$$\varepsilon = \begin{cases} \dfrac{\sigma}{E} & if \sigma < \sigma_0 \\ \dfrac{\sigma}{E} + (\dfrac{\sigma - \sigma_0}{H_b})^{1/h_b} & if \sigma > \sigma_0 \end{cases} \tag{4.3}$$

Table 4.2 presents the Ramberg-Osgood parameters calculated and figure 4.18 presents the experimental curve with the analytical curve.

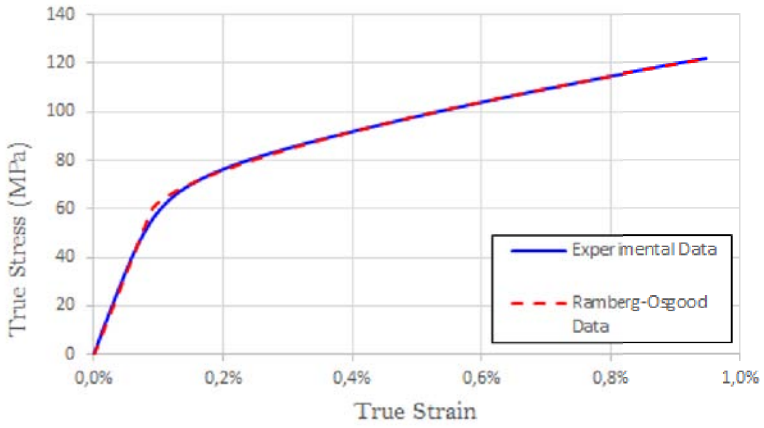

Figure 4.18: Ramberg-Osgood stress-strain curve of Aluminum alloy

5
Results

5.1
Environmentally Assisted Short Crack at Notched Specimen Results

The model to predict the non-propagating short environmental assisted crack at notch tip was validate using the metal environmental pair steel and hydrogen sulfide in accordance with section 4.1.

The experiments were carried out in DCT specimens as per ASTM 1820 [25] with $W = 55.9mm$ and $B = 8mm$ and different notches as per figure 5.1. The specimens were made from AISI 4140 steel described in section 4.1.1.

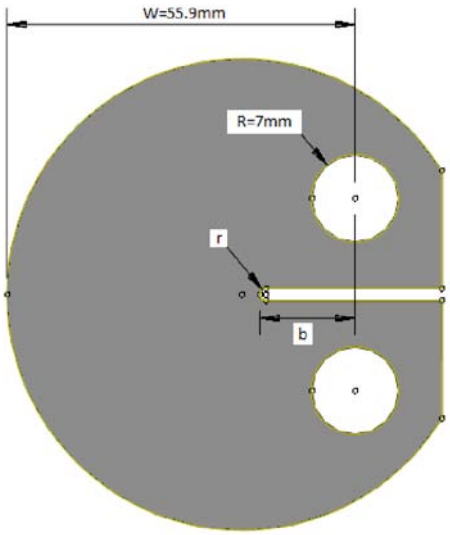

Figure 5.1: DCT standard specimen.

5.1.1
Environmentally Assisted Short Crack at Linear Elastic Regime

The determination of cracks may be difficult since the cracks can be small, sparse or obscured by corrosion deposits [27]. In this way, to validate the linear elastic model that predicts the short crack behavior at notch tip more quantitatively, the load to initiate a non-propagating crack and the load to break the specimen will be assessed considering the methodology presented in section 3.2.

The DCT specimen dimensions are based on the linear elastic model validity. In accordance with equation 2.10 from section 2.2 the main dimensions of the specimen should be bigger than $2.5(K_{SCC}/\sigma_{y0})^2$, which with the steel properties detailed in section 4.1.1 is 7.8*mm* to consider the linear elastic model.

The loads to break or to induce non-propagating crack will be assessed based on the short crack stress intensity factor curve in comparison with the stress intensity factor threshold measure in the aggressive environment considered.

Four specimens are detailed in table 5.1, which presents the specimen dimensions, the load applied, the stress in the notch root and the induced crack length.

Table 5.1: Linear Elastic DCT specimens

CP	W (mm)	B (mm)	b (mm)	ρ (mm)	P (N)	σ (MPa)	σ/S_{SCC}	$K_{short-min}/K_{th}$	a (mm)
1	55.9	8.0	15.0	2.0	6750	470.0	1.4	0.92	2.1
2	55.9	8.0	15.0	2.0	8250	574.5	1.7	1.12	∞
3	55.9	8.0	15.0	3.0	6650	378.4	1.1	0.90	1.7
4	55.9	8.0	15.0	3.0	8130	462.7	1.4	1.10	∞

The plots with the stress intensity factor by crack length extracted from *Abaqus* and the short crack stress intensity factor, blue curve, compared to the stress intensity factor threshold, dotted red curve, are presented in figures 5.2 and 5.3 for the notch with 2*mm* radius and figures 5.4 and 5.5 for 3*mm* radius notch.

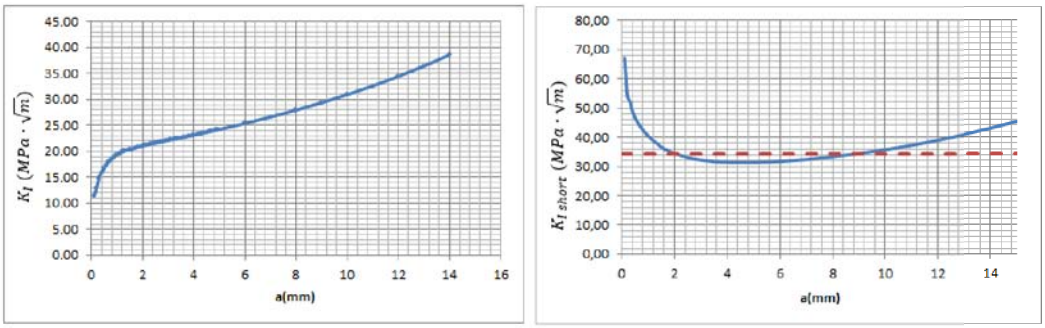

Figure 5.2: CP1 - specimen with ρ=2mm with load to induce non-propagating crack

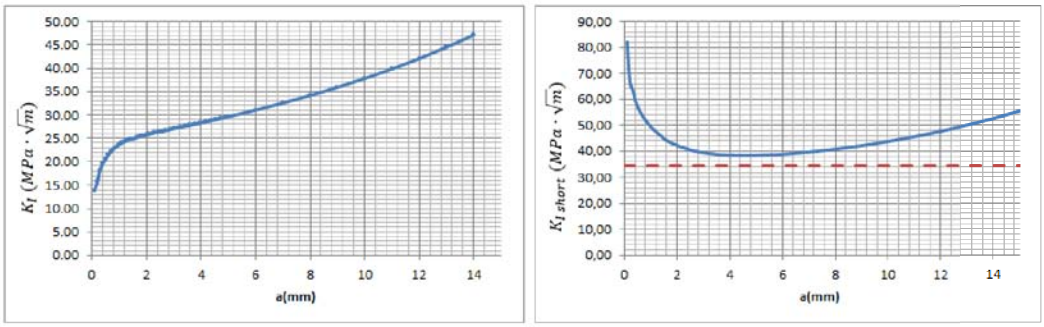

Figure 5.3: CP2 - specimen with ρ=2mm loaded to break

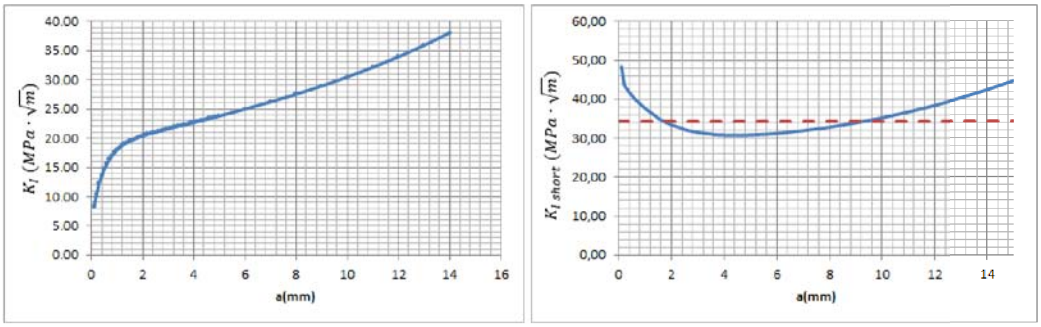

Figure 5.4: CP3 - specimen with ρ=3mm with load to induce non-propagating crack

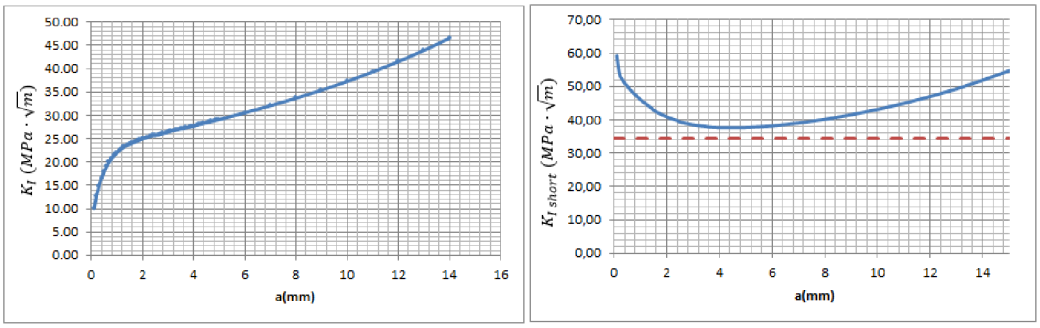

Figure 5.5: CP4 - specimen with ρ=3mm with load to induce propagating crack

Based on these plots, specimen 1 and 3 induce a non-propagating crack in the specimen notch, since the stress in the notch root are bigger than the initiation crack threshold in the considered environment (S_{SCC}) and the short crack stress intensity factor curve start above the stress intensity factor threshold, reaching the propagation crack threshold value at a non-propagating crack length detailed in table 5.1.

In the other hand, the specimen 2 and 4 will break considering the applied

load since the whole short crack stress intensity factor curve are above the stress intensity factor threshold.

Specimen 1 and 2 are tested in accordance with the experimental procedure detailed in section 4.1 to validate the proposed methodology. The results are in accordance with the prediction as per figure 5.6 that shows the specimens after 30 days of exposure to hydrogen sulfide environment at the load detailed in table 5.1. As predicted above, the specimen 1 does not break whereas the specimen 2 breaks.

Figure 5.6: CP1 and CP2 after 30 days in hydrogen sulphide environment

5.1.2 Environmentally Assisted Short Crack at Elastic Plastic Regime

Considering the J-integral model to assess short cracks from notch tip at elastic-plastic regime presented in sections 2.4 and 3.2, six DCT specimens were projected considering the steel AISI 4140 in hydrogen sulfide environment properties similar to the linear elastic specimens presented in section 5.1.1 above.

Table 5.2 presents the DCT specimens dimensions, the load considered, the stress in the notch root and the non-propagating crack length.

All the specimen presented in table 5.2 are in the plastic regime, since the stress at notch root is higher than the yielding stress which is $609MPa$ for the AISI 4140 steel as per section 4.1.1.

The J-integral by the crack length from *Abaqus* model for each geometry and load detailed in table 5.2 are presented in figures 5.7 to 5.12 with the short crack J-integral, blue curve, and the J-integral threshold in H_2S environment, dotted red curve, used to define the expected non-propagating crack behavior.

Table 5.2: Elastic Plastic DCT specimens

CP	W (mm)	B (mm)	b (mm)	r (mm)	P (N)	σ (MPa)	σ/S_{SCC}	a (mm)
1	55.9	8.0	15.0	0.2	3100	667.3	2.0	0.0
2	55.9	8.0	15.0	0.3	6000	676.2	2.0	0.5
3	55.9	8.0	15.0	0.5	7000	646.0	1.9	0.7
4	55.9	8.0	15.0	0.5	12000	768.0	2.3	∞
5	55.9	8.0	20.0	0.5	6000	658.0	2.0	0.8
6	55.9	8.0	20.0	0.5	10000	774.0	2.3	∞

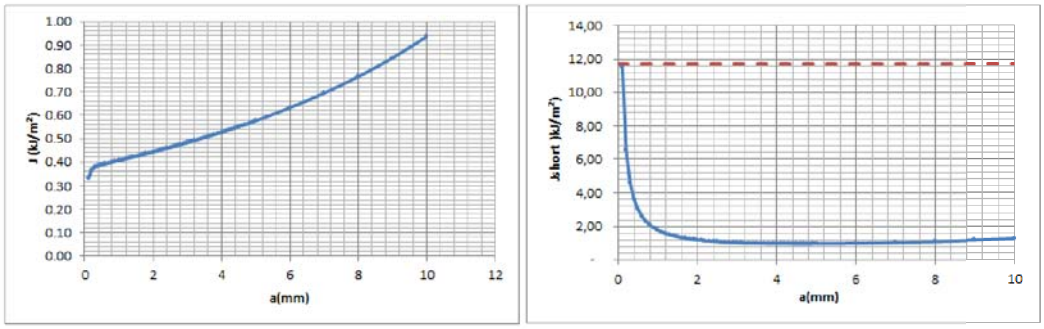

Figure 5.7: CP1 - specimen with ρ=0.2mm, b=15mm and P=3100N

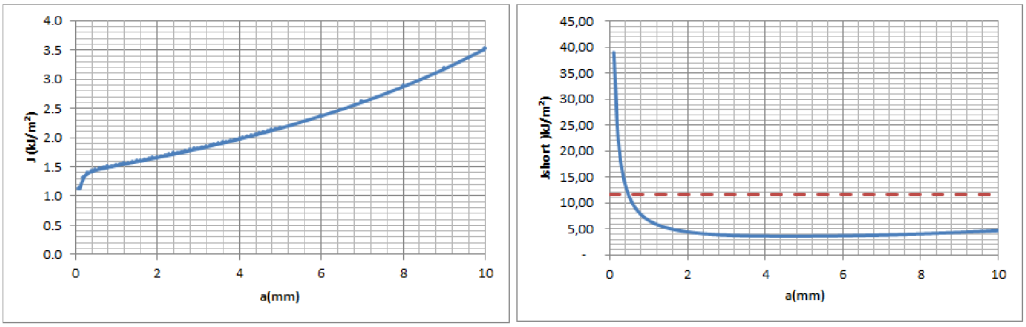

Figure 5.8: CP2 - specimen with ρ=0.3mm, b=15mm and P=6000N

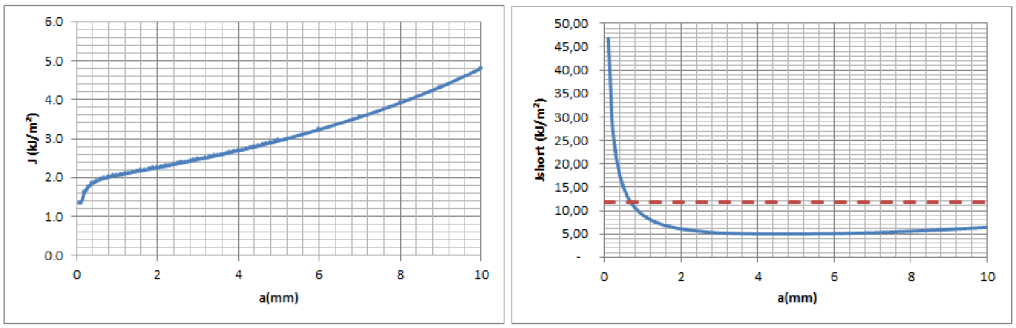

Figure 5.9: CP3 - specimen with r=0.5mm, b=15mm and P=7000N

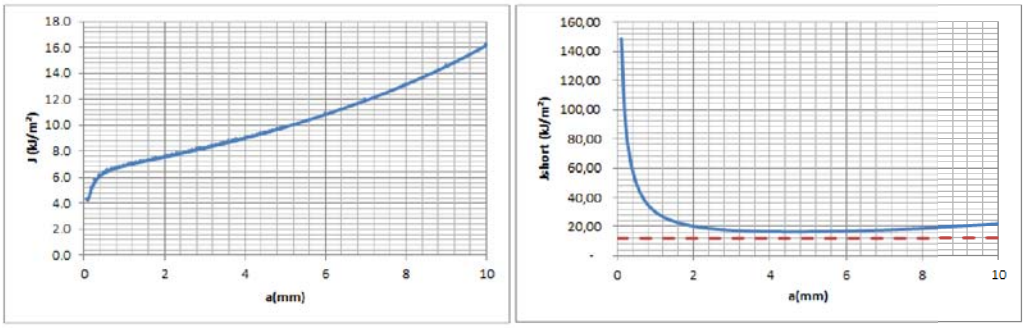

Figure 5.10: CP4 - specimen with r=0.5mm, b=15mm and P=10000N

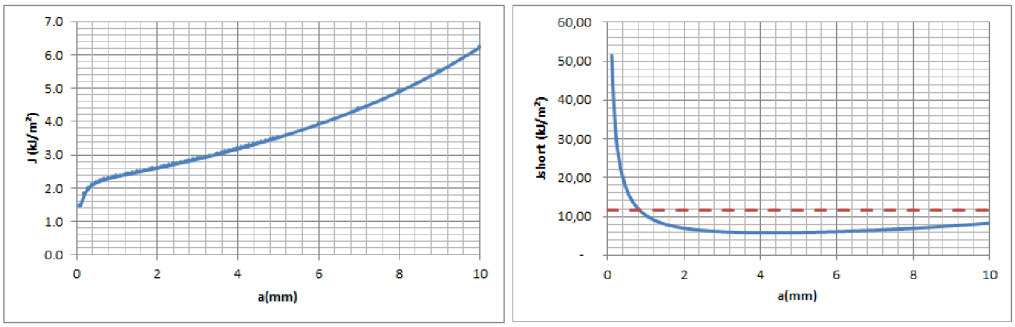

Figure 5.11: CP5 - specimen with r=0.5mm, b=20mm and P=6000N

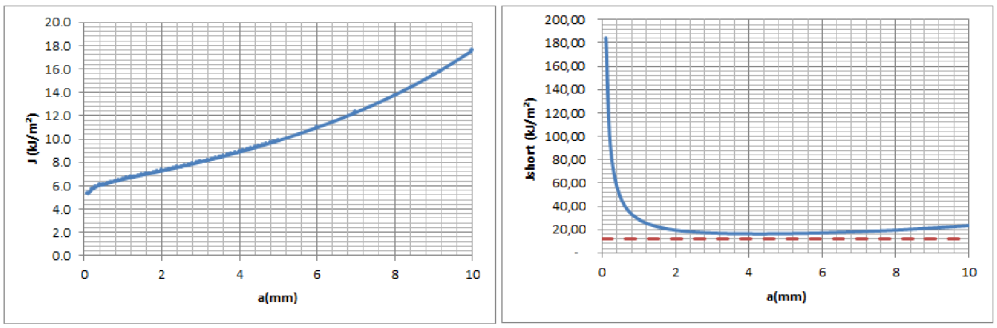

Figure 5.12: CP6 - specimen with r=0.5mm, b=20mm and P=10000N

Based on the above plots, the specimens 1, 2, 3 and 5 induce a non-propagating crack since the J-integral short curve starts above the J-integral threshold, initiating a crack that will become non-propagating when the curve reaches the J-integral threshold value.

Whereas the applied load at specimens 4 and 6 are estimated to break the specimen, since the whole J-integral short curve is above the J-integral threshold.

The specimen 3 and 4, and, 5 and 6 have the same dimensions, but the load for the first will initiate a non-propagating crack whereas the second the predict applied load will break the specimen. These comparison aims to validate more quantitatively the proposed model.

The specimen 1 and 2 are tested in accordance with the experimental

procedure detailed in section 4.1 to validate the proposed stress corrosion crack behavior in the elastic-plastic regime model. Both specimens are loaded in aqueous hydrogen sulfide environment during 30 days, and as predicted by the model, none of the specimens breaks.

Figure 5.13 presents the specimen 1 and 2 after the test.

Figure 5.13: CP1 and CP2 after 30 days in hydrogen sulfide environment

5.2 Residual Stress Results

A total of eight specimens made of Aluminum 2024 T351 described in section 4.2.4 are tested following the section 4.2 procedure.

To analyze the effect of the residual stress in the Liquid Metal Embrittlement (LME) resistance, three specimens are kept without residual stress, three receive compressive residual stress whereas two specimens are induced with tractive residual stress in the face that receives the Gallium.

Table 5.3 presents the eight specimens dimensions, thickness, wide and length measured using a caliper rule, the plastic deformation imposed in each specimen (ε), the residual strain (ε_{res}) read in the strain gauge after unloading the specimen and the calculated residual stress (σ_{res}) using section 3.2 methodology.

Table 5.3: Residual stress specimen data

CP	B (mm)	W (mm)	L (mm)	ε $(\mu m/m)$	ε_{res} $(\mu m/m)$	σ_{res} (MPa)
1	5.0	14.9	110.2	0	0	0
2	5.1	15.1	110.3	0	0	0
3	4.9	15.0	110.0	0	0	0
4	4.9	14.9	109.7	-3000	-1105	-42.6
5	4.5	14.9	109.6	-3000	-1084	-44.0
6	4.9	14.9	109.6	-3000	-1052	-46.2
7	4.9	14.9	109.5	3042	1113	45.2
8	4.8	14.9	109.8	3000	1061	46.2

After the residual stress imposed following table 5.3 data, the Gallium was applied to the specimens and they are loaded in a slow strain rate in accordance with 4.2.3 procedure.

The stress and strain history are assessed considering the Ramberg-Osgood relation defined in section 4.2.4 and is considered that the stress-strain curve of the Aluminum does not change during the Liquid Metal Embrittlement process, as stated by Kamdar [28].

For this case, the simplified assessment considering the elastic perfectly plastic material model detailed in section 3.2 are not recommended since high plastic strains are applied to the specimens.

The breaking load under liquid metal embrittlement of Aluminum specimens with Gallium and the stress and strain history of each specimen are presented in the tables and figures below. The residual stress loading and unloading are represented by the dotted red curve and the LME loading is the blue curve in the following figures.

The breaking stress (σ_{break}) and strain (ε_{break}) stated in the results corresponds to the stress and strain considering the entire loading history since the applied residual stress imposed before the Gallium whereas the breaking load (P_{break}) is the load applied in the specimens after Gallium application.

Table 5.4 presents the breaking load and stress and strain history of the specimens that do not receive residual stress whereas figure 5.14 shows the stress and strain history plot and figure 5.15 the stress profile when the specimen breaks.

Table 5.5: Results from specimens induced with compressive residual stress

CP	P_{break} (N)	ε $(\mu m/m)$	σ (MPa)	ε_{res} $(\mu m/m)$	σ_{res} (MPa)	ε_{break} $(\mu m/m)$	σ_{break} (MPa)
4	497	-3000	84.5	-1105	-42.6	2670	62.9
5	459	-3000	84.5	-1084	-44.0	2790	71.0
6	552	-3000	84.5	-1052	-46.2	2810	72.4

Table 5.4: Results of specimens without residual stress

CP	P_{break} (N)	ε_{break} $(\mu m/m)$	σ_{break} (MPa)
1	641	2950	84.2
2	674	2950	84.2
3	583	2550	80.9

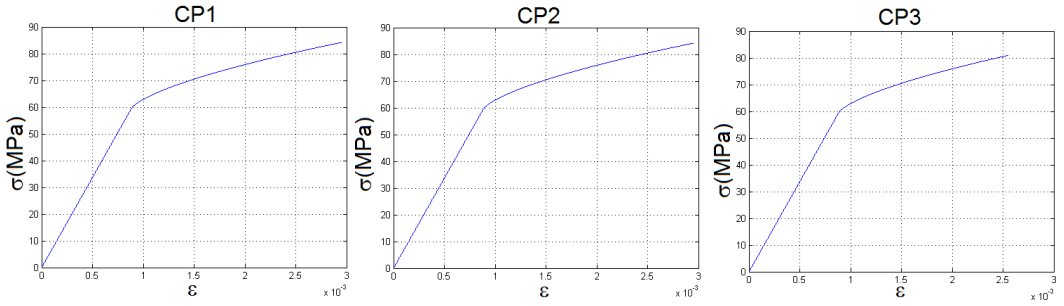

Figure 5.14: Stress and strain history - specimens without residual stress

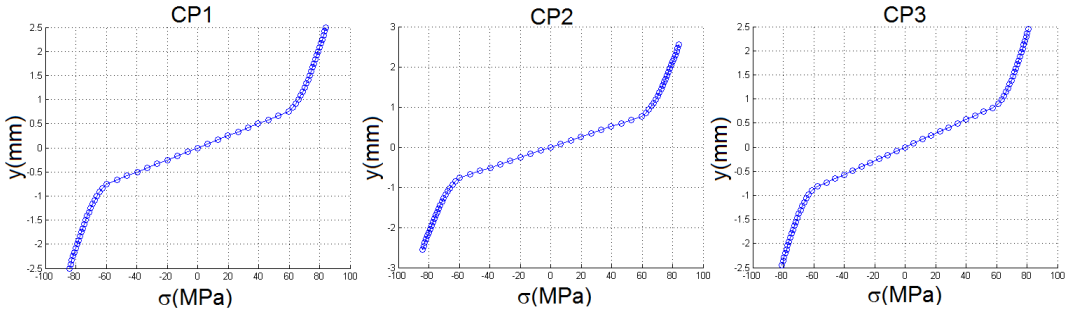

Figure 5.15: Stress profile when the specimen breaks - specimens without residual stress

Table 5.5 presents the results for the specimens that receive the compressive residual stress. The stress and strain history for these specimens are presented in figure 5.16 and the stress profile on figure 5.17.

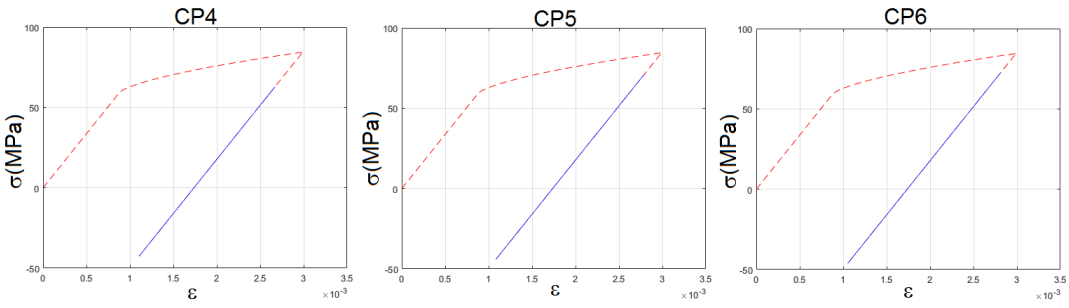

Figure 5.16: Stress and strain history - specimens with compressive residual stress

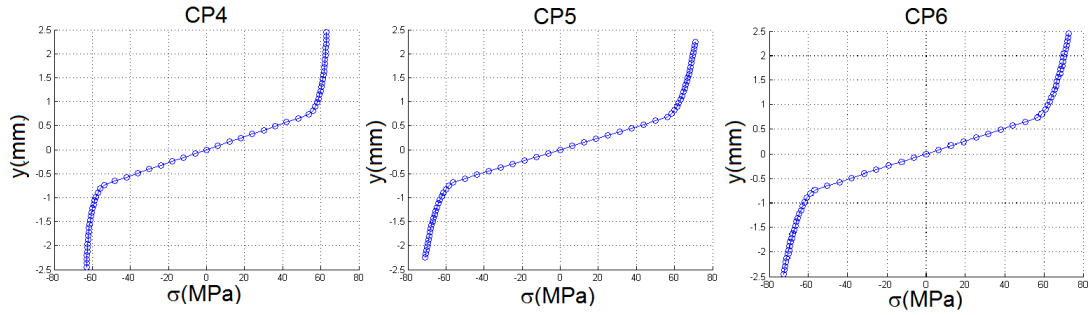

Figure 5.17: Stress profile when the specimen breaks - specimens with compressive residual stress

Therefore, table 5.6 presents the results for the specimens that receive the tractive residual stress, the figure 5.18 presents the stress and stress history and the figure 5.19 presents the final stress profile for these specimens.

Table 5.6: Results from specimens induced with tractive residual stress

CP	P_{break} (N)	ε $(\mu m/m)$	σ (MPa)	ε_{res} $(\mu m/m)$	σ_{res} (MPa)	ε_{break} $(\mu m/m)$	σ_{break} (MPa)
7	471	3042	84.9	1113	45.1	30	88.6
8	403	3000	84.5	1061	45.5	190	86.7

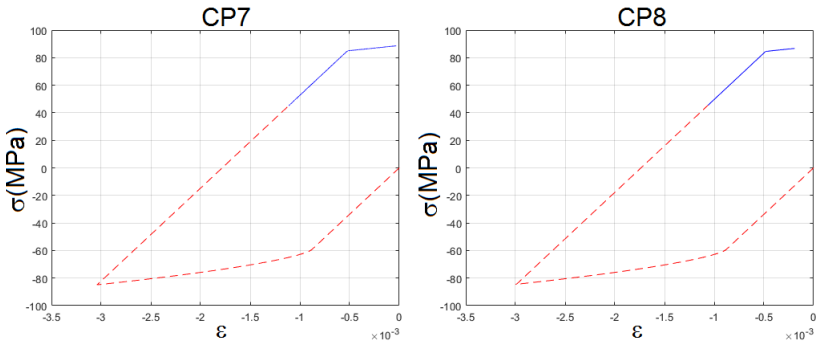

Figure 5.18: Stress and strain history - specimens with tractive residual stress

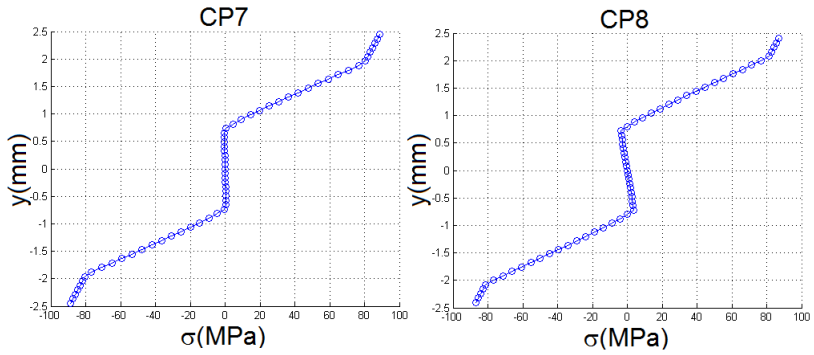

Figure 5.19: Stress profile when the specimen breaks - specimens with tractive residual stress

The average and standard deviation of the results (loading to break applied after Gallium application, stress and strain until specimens break considering the loading history from load applied to induce the residual stress) for each case (without residual stress, with compressive and tractive residual stress) are presented in table 5.7.

Table 5.7: Average results

Residual Stress	P_{break} (N)	ε_{break} $(\mu m/m)$	σ_{break} (MPa)
Without	633 ± 46	2817 ± 231	83 ± 2
Compressive	503 ± 47	2757 ± 76	69 ± 5
Tractive	437 ± 48	110 ± 113	88 ± 1

Figure 5.20 presents some of the specimens after the experiment.

Based on the results presented in table 5.7, it can be concluded that the stress and strain state when the specimens breaks are not the same for the different residual stress imposed, not allowing to define a threshold stress or strain for the EAC of the Aluminum in Gallium environment.

Figure 5.20: Specimens after stress corrosion cracking

However, as the load to break for the specimens with residual stress induced by plastic deformation (tractive and compressive) are small than the load to break the specimen without the residual stress , it can be concluded that the induced plastic deformation decrease the resistance of the Aluminum specimens in the LME by Gallium, even for the compressive residual stress induced.

This can be explained by the discontinuity density that increases due to the induced plastic deformation and changes the ductility of the material in accordance with Reed-Hill [57] . Since, as the annealing it was necessary to have measurable stress corrosion cracking resistance of the aluminum plate in Gallium environment in accordance with Landim [56], it can be implied that the effectiveness of the annealing process to increase the stress corrosion cracking resistance it was due to the decreasing of dislocation density during the process instead of the direct decrease of residual stress induced by the cold work.

Another explanation can be the liquid metal embrittlement dissolution processes that bring the Gallium from the compressive residual stress face to the tractive residual stress face of the bending specimen, initiating the crack to break by the tractive face with a lower load than the specimen without residual stress.

In despite the literature assert that compressive residual stress has a beneficial effect on stress corrosion cracking, the experiments carried out on this work shows that caution is necessary when threat the effect of residual stress on SCC since the residual stress could not be considered as an external stress and the metallurgical facts could not be disregarded.

Therefore, it is not the aim of this work to go deep in the metallurgical of stress corrosion cracking phenomena.

6
Conclusion

The effect of elastic-plastic stress, based on mechanical approach and fracture mechanics theory was extended to the stress corrosion cracking problem to evaluate the resistance of a structure under SCC conditions.

This work presents two fronts to validate the use of the mechanical approach to the stress corrosion cracking problem phenomena.

The first, which analyze the behavior of short crack under linear elastic and elastic-plastic regime in compact tension notched specimens, validated using AISI 4140 steel in aqueous hydrogen sulphide pair, present consistent results showing that the proposed model are robust to predict the critical stress that a notched structure can withstand under environment assisted cracking condition.

Moreover, this work should be extended to other metal environmental pair and other specimen geometries, also in the elastic plastic regime as already proposed by Landim [56] and Leite [46].

Furthermore, the second front, analyze the residual stress influence in the liquid metal embrittlement threshold of Aluminum specimens in Gallium environment. In this front, the proposed model is not successful, making it clear that the metallurgical effects, in this case, must not be disregarded. However, this methodology should be, in the future, studied for others metal environmental pairs with the care in the metallurgical and microstructure phenomena.

Therefore, the use of a model that considers the applied stress and evaluate the corrosion effects under the material properties can be used to external load applied to structures, as the prediction of non-propagating crack behavior departing from notch tips studied in this work, but, the effect of non-external applied stress, as the residual stress, that changes the metallurgic properties of the material, could not be studied through this simplified mechanical model.

7
Bibliography

[1] DIETZELM W. Fracture Mechanics Approach to Stress Corrosion Cracking. Anales de Mecánica de la Fractura, v.18, 2001

[2] POPOV, B.N. Corrosion Engineering: Principles and Solved Problems. 1.ed.. Amsterdam: Elsevier B.V., 2015

[3] FONTANA, M.G.Fontana Corrosion Engineering. 3.ed. New York: McGraw-Hill Book Company, 1987.576p.

[4] ASTM INTERNATIONAL ASTM E1681-03: Standard Test Method for Determine Threshold Stress Intensity Factor for Environment-Assisted Cracking of Metallic Materials. West Conshohocken, 2013

[5] ASTM INTERNATIONAL ASTM F1624-09: Standard Test Method for Measurement of Hydrogen Embrittlement Threshold in Steel by the Incremental Step Loading Technique. West Conshohocken, 2009

[6] DIETZEL, W.; SCHWALBE, K.H.; WU, D. Application of Fracture Mechanics Techniques to the Environmentally Assited Cracking of Aluminium 2024. Fatigue & Fracture of Engineering Materials & Structures, v.12, n.6, p.495-510, 1989

[7] PENG, Q.J.; KWON, J.; SHOJI, T.Development of a fundamental crack tip strain rate equation and its application to quantitative prediction of stress corrosion cracking of stainless steel in high temperature oxygenated water Journal of Nuclear Materials, v.324, p. 52-61, 2004

[8] ABRAMSON,G.; EVANS, J.T.; PARKINS, R.N. Investigation of Stress Corrosion Crack Growth in Mg Alloys Using J-integral Estimations. Metallurgical Transactions, v. 16A, p.101-108, 1985

[9] SADANANDA, K.; VASUDEVAN, A.K.Failure Diagram for Chemically Assisted Crack Growth. Metallurgical and Materials Transactions, v. 42A, p.296-303, 2011

[10] Status Review of Initiation of Environmentally Assisted Cracking and Short Crack Growth. Palo Alto: Eletric Power Research Institute, 2005.Technical Report 1011788

[11] CASTRO, J.T.P.; et. al. Prediction of fatigue crack initiation lives at elongated notch roots using short crack concepts. International Journal of Fatigue, v.42, p.172-182, 2012

[12] CASTRO, J.T.P.; MEGGIOLARO, M.A. Is notch sensitivity a stress analysis problem? Fratturaned Integritá Strutturale,v.25, p.79-86, 2013

[13] MEGGIOLARO, M.A.; MIRANDA, A.C.O.; CASTRO, J.T.P. Short Crack threshold estimates to predict notch sensitivity factors in fatigue. International Journal of Fatigue,v.29, p.2022-2031, 2007

[14] CASTRO, J.T.P., et.al. Prediction of notch sensitivity effects in fatigue and in environmentally assisted cracking. Fatigue and Fracture of Engineering Materials and Structures,v.38, n.2, p.161-179, 2015

[15] CASTRO, J.T.P; LANDIM, R.V.; MEGGIOLARO, M.A. Defect Tolerance under Environmentally-Assisted Cracking Conditions., Corrosion Reviews,v.33, n.6,p.417-431, 2015

[16] EL HADDAD, M.H.; TOPPER, T.H.; SMITH, K.N. Prediction of non propagating cracks. Engineering Fracture Mechanics, v. 11, n. 3, p. 573-584, 1979

[17] EL HADDAD, M.H. et. al. J-integral applications for short fatigue cracks at notches. International Journal of Fracture, v.16,n.1,p.15-30, 1980

[18] CASTRO, J.T.P; MEGGIOLARO, M.A.Fadiga: Técnicas e Práticas de Dimensionamento Estrutural sob Cargas Reais de Serviço.1.ed. San Bernardino: Amazon, 2013

[19] TADA, H.; PARIS, P.C.; IRWIN, G.R. The Stress Analysis of Cracks Handbook 3.ed. New York: ASME International, 2000. 698p.

[20] ASTM INTERNATIONAL. ASTM E399-12: Standard Test Method for Linear-elastic Plane-strain Fracture Toughness K_{IC} of Metallic Materials. West Conshohocken, 2012

[21] RICE, J.R. A Path Independent Integral and the Approximate Analysis of Strain Concentration by Notches and Cracks. Journal of Applied Mechanics, v.35, p. 379-386, 1968

[22] HUTCHINSON, J.W. Plastic Stress and Strain Fields at Crack Tip. J.Mech.Phys.Solids, v.16, p,337-347, 1968

[23] GOLDMAN, N.L.; HUTCHINSON,J.W. Fully Plastic Crack Problems: the center-crackes strip under plane strain. International Journal of Solids Structures,v.11, p.575-591, 1975

[24] SHIH, C.F.; HUTCHINSON, J.W. Fully Plastic Solutions and Large Scale Yielding Estimates for Plane Stress Crack Problems. Journal of Engineering Materials and Technology, v.98, p.289-295, 1976

[25] ASTM INTERNATIONAL. ASTM E-1820-13: Standard test Method for Measurement of Fracture Toughness. West Conshohocken , 2014

[26] NEWMAN, R.C. Corrosion Mechanisms in Theory and Practice: Stress corrosion cracking mechanisms. 2.ed. New York: Marcel Dekker Inc.1995.51p.

[27] NACE INTERNATIONAL NACE TM0177: Laboratory Testing of Metals for Resistance to Sulfide Stress Cracking and Stress Corrosion Cracking in H_2S Environments., Houston, 2005

[28] KAMDAR, M.H.Embrittlement by Liquid Metals. Progress in Materials Science, v.15, n.4,p.289-374, 1973

[29] JOSEPH, B.; PICAT, M.; BARBIER, F.Liquid metal embrittlement: A state-of-the-art appraisal. The European Physical Journal Applied Physics, v.5, p.19-31, 1999

[30] SADANANDA, K.; VASUDEVAN, A.K. Review of Environmentally Assisted Cracking. Metallurgical and Materials Transactions A, v.42, n.2, p.279-295, 2011

[31] NICHOLAS, M.G. ; OLD, C.F. Review Liquid Metal Embrittlement. Journal of Materials Science, v.14, p.1-18, 1979

[32] BENSON, B.A.; HOAGLAND, R.G. Crack Growth Behavior of a high strength aluminum alloy during LME by Gallium. Scripta Metallurgica, v.23, p.1943-4948, 1989

[33] VASUDEVAN, A.K. Applied Stress Affecting the Environmentally Assisted Cracking. Metallurgical and Materials Transactions A, v.44, n.3, p.1254-1267, 2013

[34] FLAMINI, D.O.; SAIDMAN, S.B.;BESSON,J.B. Aluminium Activation produced by Gallium. Corrosion Science,v.48, p. 1413-1425, 2006

[35] DESRE, P.J. A mechanism for the stress independent grain boundary penetration of a metal by a liquid metal. Application to the metallic couple Al-Ga. Scripta Materialia, v.37, n.6, p.875-881, 1997

[36] LASMIS, J.L. Prestress Engineering of Structural Material: A Global Design Approach to the Residual Stress Problem. Handbook of Residual Stress and Deformation of Steel - ASM International, p.11-26, 2002

[37] NUNES, R.M. Análise de tensões residuais no processo de trefilação combinada do aço AISI 1048 visando minimizar distorções pos processamento. Porto Alegre, 2008.124p. Dissertação de Mestrado - Engenharia de Minas, Metalúrgica e de Materiais. Universidade Federal do Rio Grande do Sul.

[38] HUTCHINGS, M.T. et. al. Introduction to the Characterization of Residual Stress by Neutron Diffraction. 1ed. cidade: CRCPress, 2005. 420p.

[39] PARKS, D.M. The virtual crack extension method for non-linear material behavior. Computer Methods in Applied Mechanics and Engineering, v.12, p.365-364, 1977

[40] VETHE, S. Numerical Simulation of Fatigue Crack Growth. Trondheim, 2012. 53p. Master Thesis - Department of Engineering Design and Materials, Norwegian University of Science and Technology.

[41] DASSAULT SYSTÈMES. Abaqus/CAE: User Guide. Version 6.13-1, 2013. Eletronic report available in Abaqus environment.

[42] SIMHA, N.K. et. al. J-integral and crack driving force in elastic-plastic materials. Journal of the Mechanics and Physics of Solids, v.56, p.2876-2895, 2008

[43] BARSOUM,R.S. Triangular quarter-point element as elastic and perfectly-plastic crack tip elements. International Journal for Numerical Methods in Engineering, v.11, p. 85-98, 1977

[44] Fracture Mechanics Study of a Compact Tension Specimen Using Abaqus/CAE. Providence: Dassault Systèmes, 2007. Abaqus Technology Brief TB-04-FMCAE-1

[45] MIRANDA, A.C.O. Propagação de Trincas por Fadiga em Geometrias 2D Complexas sob Cargas Cíclicas Variáveis. Rio de Janeiro, 2003.125p. Tese de Doutorado - Engenharia Civil, Pontifícia Universidade Católica do Rio de Janeiro.

[46] LEITE, J.C.C. Notch sensitivity in environmentally assisted cracking (EAC) - methodologies and specimens analysis.Rio de Janeiro, 2014. 134p. Tese de Mestrado - Engenharia Mecânica, Pontifícia Universidade Católica do Rio de Janeiro.

[47] RUSMEE, P. High Strength Composites [Internet]. Salt Lake City: The University of Utah, Department of Mechanical Engineering; [Updated in Sep 2005; cited in Jun 2015]. Available in: http://www.mech.utah.edu/ rusmeeha/labNotes/composites.html

[48] JOHNSON, W. ; MELLOR, P. P. B. Enginnering Plasticity. 1.ed. Van Nostrand Reinhold Inc, 1978, 646p.

[49] SIMO, J.C.; HUGHES, T.J.R Computational Inelasticity.1.ed. New York: Springer-Verlag, 1997, 404p.

[50] ASTM INTERNATIONAL ASTM G1: Standard Practice for Preparing, Cleaning, and Evaluating Corrosion Test Specimens. West Conshohocken, 2011

[51] ASM Handbook Materials Handbook 2030

[52] BRADY, G.S. ; CLAUSER, H.R.; VACCARI, J.A.Materials Handbook. 15.ed.New York: McGraw-Hill, 2012

[53] ASTM INTERNATIONAL ASTM E8/E8M-13a: Standard Test Methods for Tension Testing of Metallic Materials. West Conshohocken, 2013

[54] ASTM INTERNATIONAL ASTM G39-99: Standard Practice for Preparation and Use of Bent-Beam Stress-Corrosion Test Specimen West Conshohocken, 2011

[55] ASTM INTERNATIONAL ASTM G129-00: Standard Practice for Slow Strain Rate Testing to Evaluate the Susceptibility of Metallic Materials to Environmentally Assisted Cracking West Conshohocken, 2000

[56] LANDIM, R.V. Efeito da Sensibilidade ao Entalhe em Condições de Trincamento Assistido por Meios Corrosivos. Rio de Janeiro, 2013. 116p. Tese de Mestrado - Engenharia Mecânica, Pontifícia Universidade Católica do Rio de Janeiro.

[57] ABBASCHIAN, R.; ABBASCHIAN, L.; REED-HILL, R.E.Physical Metallurgy Principles. 4.ed. Stamford: Cengoge Learning, 2009.769p.

A
Phyton Code - Linear Elastic

```
from abaqus import*
from abaqusConstants import*
import part, material, section, assembly, step, interaction
import regionToolset, displayGroupMdbToolset as dgm, mesh, load, job
import optimization, sketch, visualization, xyPlot, connectorBehavior,
displayGroupOdbToolset as dgo
##=====================================================================
## INPUT
##=====================================================================

b0=15

#Open the CAE model
=======================================================================
mdb=openMdb('CT_standard_crack' +'.cae')

#Output read
=======================================================================

outputRes = open('CrackResults.txt','a')

firstLine=['Crack'," ",'KI',"\n"]
outputRes.writelines(firstLine)
outputRes.close()


for c in range(1,61):

        if c<51:

                a=0.1*c

        else: a=c-45

#Copying the basic model

mdb.Model(name='Global_crack-
growth_'+str(c)+'mm',objectToCopy=mdb.models['Global_crack-gr owth_phyton'])
myModel=mdb.models['Global_crack-growth_'+str(c)+'mm']
myAssembly=myModel.rootAssembly myPartInstance=myAssembly.instances['CT-1']
myMaterial=myModel.materials['STEEL']

#Creating the crack partitions
CrackMeshSketch=myModel.ConstrainedSketch(name='Crack_Mesh_Sketch', sheetSize=
200.0)

#Inserting the 2 cycles and the line for the crack front
CrackMeshSketch.CircleByCenterPerimeter(center=(-a-b0,0),point1=(-b0,0))
CrackMeshSketch.CircleByCenterPerimeter(center=(-a-b0,0),point1=(-b0+3.865,1.25))
CrackMeshSketch.Line(point1=(-b0,0),point2=(-a-b0,0))

Faces1=myPartInstance.faces.findAt((-30,10,0))

myAssembly.PartitionFaceBySketch(faces=Faces1, sketch=CrackMeshSketch)

Faces2=myPartInstance.faces.findAt((-30,-10,0))
```

```
myAssembly.PartitionFaceBySketch(faces=Faces2, sketch=CrackMeshSketch)

CrackEdge=myPartInstance.edges.findAt(((-b0-0.5*a, 0.0, 0.0),))

CrackEdgeSet=myAssembly.Set(edges=CrackEdge,name='Crack')

myAssembly.engineeringFeatures.assignSeam(regions=CrackEdgeSet)

CircleSup = myPartInstance.faces.findAt(((-a-b0, 0.05*a, 0), ),((-a-b0, 0.06*a, 0), ),((-b0,
1, 0), ))

myAssembly.setMeshControls(regions=CircleSup, elemShape=QUAD_DOMINATED,
technique=SWEEP)

CircleInf = myPartInstance.faces.findAt(((-a-b0, -0.05*a, 0), ),((-a-b0, -0.06*a, 0),),((-b0, -
1, 0), ))

myAssembly.setMeshControls(regions=CircleInf, elemShape=QUAD_DOMINATED,
technique=SWEEP)

Allpart=(myPartInstance,) myAssembly.generateMesh(regions=Allpart)

CrackVert=myPartInstance.vertices.findAt(((-a-b0, 0, 0), ),((-a-b0,0 ,0 ), ),((-a-b0,0 ,0 ), ))
CrackFront = regionToolset.Region(vertices=CrackVert)

myAssembly.engineeringFeatures.ContourIntegral(name='Crack-1', symmetric=OFF,
crackFront=CrackFront, crackTip=CrackFront,
        extensionDirectionMethod=Q_VECTORS, qVectors=(((-a-b0, 0.0, 0.0), (-a-b0-a,
0.0, 0.0)), ),
                midNodePosition=0.25,
                collapsedElementAtTip=SINGLE_NODE)


myModel.HistoryOutputRequest(name='Crack-Output',
        createStepName='Static', contourIntegral='Crack-1',
        sectionPoints=DEFAULT, rebar=EXCLUDE, numberOfContours=5,
        contourType=K_FACTORS, kFactorDirection=MERR)

myAssembly.regenerate()

myJob = mdb.Job(name='Global_crack-growth_'+str(c)+'mm',
model='Global_crack-growth_'+str(c)+'mm',description='Contour integral analysis')
myJob.submit(consistencyChecking=OFF)

myJob.waitForCompletion()

session.mdbData.summary()

o1 = session.openOdb(name='Global_crack-growth_'+str(c)+'mm.odb')

session.viewports['Viewport: 1'].setValues(displayedObject=o1)

odb = session.odbs['Global_crack-growth_'+str(c)+'mm.odb']

xy0 = xyPlot.XYDataFromHistory(odb=odb,
        outputVariableName='Stress intensity factor K1: K1 at
```

```
        CRACK-OUTPUT_CRACK-1__PICKEDSET48_Contour_2 in ELSET  ALL ELEMENTS',
        steps=('Static', ), suppressQuery=True)
xy1 = xyPlot.XYDataFromHistory(odb=odb,
        outputVariableName='Stress intensity factor K1: K1 at
        CRACK-OUTPUT_CRACK-1__PICKEDSET48_Contour_3 in ELSET  ALL ELEMENTS',
        steps=('Static', ), suppressQuery=True)

xy2 = xyPlot.XYDataFromHistory(odb=odb,
        outputVariableName='Stress intensity factor K1: K1 at
        CRACK-OUTPUT_CRACK-1__PICKEDSET48_Contour_4 in ELSET  ALL ELEMENTS',
        steps=('Static', ), suppressQuery=True)

xy3 = xyPlot.XYDataFromHistory(odb=odb,
        outputVariableName='Stress intensity factor K1: K1 at
        CRACK-OUTPUT_CRACK-1__PICKEDSET48_Contour_5 in ELSET  ALL ELEMENTS',
        steps=('Static', ), suppressQuery=True)

xy4 = avg((xy0, xy1, xy2, xy3, ), )

session.XYData(name='XYData-'+str(a), objectToCopy=xy4,
sourceDescription='avg((Stress intensity factor K1: K1 at CRACK-OUTPUT_CRACK-
1__PICKEDSET48_Contour_2 in ELSET  ALL ELEMENTS, Stress intensity factor K1: K1 at
CRACK-OUTPUT_CRACK-1__PICKEDSET48_Contour_3 in ELSET  ALL ELEMENTS, Stress
intensity factor K1: K1 at CRACK-OUTPUT_CRACK-1__PICKEDSET48_Contour_4 in ELSET
ALL ELEMENTS, Stress intensity factor K1: K1 at CRACK-OUTPUT_CRACK-
1__PICKEDSET48_Contour_5 in ELSET  ALL ELEMENTS, ),)')

x0 = session.xyDataObjects['XYData-'+str(a)].data[0][1]

outputRes = open('CrackResults.txt','a') Line=[str(a)," ",str(x0),"\n"]
outputRes.writelines(Line) outputRes.close()
```

B
Phyton Code - Elastic Plastic

```
from abaqus import*
from abaqusConstants import*
import part, material, section, assembly, step, interaction
import regionToolset, displayGroupMdbToolset as dgm, mesh, load, job
import optimization, sketch, visualization, xyPlot, connectorBehavior,
displayGroupOdbToolset as dgo
##=====================================================================
## INPUT
##=====================================================================

b0=15

#Open the CAE model
=======================================================================
mdb=openMdb('CT_standard_crack' +'.cae')

#Output read
=======================================================================

outputRes = open('CrackResults.txt','a')

firstLine=['Crack'," ",'J',"\n"] outputRes.writelines(firstLine) outputRes.close()

for c in range(1,2):

        if c<51:

                a=0.1*c

        else:

                a=c-45

#Copying the basic model

mdb.Model(name='Global_crack-
growth_'+str(c)+'mm',objectToCopy=mdb.models['Global_crack-gr owth_phyton'])
myModel=mdb.models['Global_crack-growth_'+str(c)+'mm']
myAssembly=myModel.rootAssembly myPartInstance=myAssembly.instances['CT-1']
myMaterial=myModel.materials['STEEL']

#Creating the crack partitions
CrackMeshSketch=myModel.ConstrainedSketch(name='Crack_Mesh_Sketch', sheetSize=
200.0)

#Inserting the 2 cycles and the line for the crack front
CrackMeshSketch.CircleByCenterPerimeter(center=(-a-b0,0),point1=(-b0,0))
CrackMeshSketch.CircleByCenterPerimeter(center=(-a-b0,0),point1=(-b0+3.732051,1))
CrackMeshSketch.Line(point1=(-b0,0),point2=(-a-b0,0))

Faces1=myPartInstance.faces.findAt((-30,10,0))

myAssembly.PartitionFaceBySketch(faces=Faces1, sketch=CrackMeshSketch)

Faces2=myPartInstance.faces.findAt((-30,-10,0))
```

```
myAssembly.PartitionFaceBySketch(faces=Faces2, sketch=CrackMeshSketch)

CrackEdge=myPartInstance.edges.findAt(((-b0-0.5*a, 0.0, 0.0),))

CrackEdgeSet=myAssembly.Set(edges=CrackEdge,name='Crack')

myAssembly.engineeringFeatures.assignSeam(regions=CrackEdgeSet)

CircleSup = myPartInstance.faces.findAt(((-a-b0, 0.05*a, 0), ),((-a-b0, 0.06*a, 0), ),((-b0,
1, 0), ))

myAssembly.setMeshControls(regions=CircleSup, elemShape=QUAD_DOMINATED,
technique=SWEEP)

CircleInf = myPartInstance.faces.findAt(((-a-b0, -0.05*a, 0), ),((-a-b0, -0.06*a, 0), ),((-b0, -
1, 0), ))

myAssembly.setMeshControls(regions=CircleInf, elemShape=QUAD_DOMINATED,
technique=SWEEP)

myAssembly.seedEdgeBySize(edges=CrackEdge, size=0.1,
deviationFactor=0.1,minSizeFactor=0.1, constraint=FINER)

Allpart=(myPartInstance,) myAssembly.generateMesh(regions=Allpart)

CrackVert=myPartInstance.vertices.findAt(((-a-b0, 0, 0), ),((-a-b0,0 ,0 ), ),((-a-b0,0 ,0 ), ))
CrackFront = regionToolset.Region(vertices=CrackVert)

myAssembly.engineeringFeatures.ContourIntegral(name='Crack-1', symmetric=OFF,
crackFront=CrackFront, crackTip=CrackFront,
        extensionDirectionMethod=Q_VECTORS, qVectors=(((-a-b0, 0.0, 0.0), (-a-b0-a,
0.0, 0.0)), ),
                midNodePosition=0.25,
                collapsedElementAtTip=DUPLICATE_NODES)

myModel.HistoryOutputRequest(name='Crack-Output',
        createStepName='Static', frequency=LAST_INCREMENT, contourIntegral='Crack-
1',
        sectionPoints=DEFAULT, rebar=EXCLUDE, numberOfContours=5)

myAssembly.regenerate()

myJob = mdb.Job(name='Global_crack-growth_'+str(c)+'mm',

model='Global_crack-growth_'+str(c)+'mm',description='Contour integral analysis')

myJob.submit(consistencyChecking=OFF)

myJob.waitForCompletion()

session.mdbData.summary()

o1 = session.openOdb(name='Global_crack-growth_'+str(c)+'mm.odb')

session.viewports['Viewport: 1'].setValues(displayedObject=o1)
```

```
odb = session.odbs['Global_crack-growth_'+str(c)+'mm.odb']

xy0 = xyPlot.XYDataFromHistory(odb=odb,
        outputVariableName='J-integral: J at CRACK-OUTPUT_CRACK-1__PICKEDSET50-
1__Contour_2 in ELSET  ALL ELEMENTS',
        steps=('Static', ), suppressQuery=True)

xy1 = xyPlot.XYDataFromHistory(odb=odb,
        outputVariableName='J-integral: J at CRACK-OUTPUT_CRACK-1__PICKEDSET50-
1__Contour_3 in ELSET  ALL ELEMENTS',
        steps=('Static', ), suppressQuery=True)

xy2 = xyPlot.XYDataFromHistory(odb=odb,
        outputVariableName='J-integral: J at CRACK-OUTPUT_CRACK-1__PICKEDSET50-
1__Contour_4 in ELSET  ALL ELEMENTS',
        steps=('Static', ), suppressQuery=True)

xy3 = xyPlot.XYDataFromHistory(odb=odb,
        outputVariableName='J-integral: J at CRACK-OUTPUT_CRACK-1__PICKEDSET50-
1__Contour_5 in ELSET  ALL ELEMENTS',
        steps=('Static', ), suppressQuery=True)

xy4 = avg((xy0, xy1, xy2, xy3, ), )

session.XYData(name='XYData-'+str(a), objectToCopy=xy4,

sourceDescription='avg((J-integral: J at CRACK-OUTPUT_CRACK-1__PICKEDSET50-
1__Contour_2
in ELSET  ALL ELEMENTS, J-integral: J at CRACK-OUTPUT_CRACK-1__PICKEDSET50-
1__Contour_3
in ELSET  ALL ELEMENTS, J-integral: J at CRACK-OUTPUT_CRACK-1__PICKEDSET50-
1__Contour_4
in ELSET  ALL ELEMENTS, J-integral: J at CRACK-OUTPUT_CRACK-1__PICKEDSET50-
1__Contour_5
in ELSET  ALL ELEMENTS, ),)')

x0 = session.xyDataObjects['XYData-'+str(a)].data[0][1]

outputRes = open('CrackResults.txt','a')
Line=[str(a)," ",str(x0),"\n"]
outputRes.writelines(Line)
outputRes.close()

session.xyDataListFromField(odb=odb, outputPosition=
        NODAL, variable=(('CF', NODAL, ((INVARIANT, 'Magnitude'), )), ('U', NODAL,
((INVARIANT,
         'Magnitude'), )), ), nodeSets=('TOP_PT', ))

U0 = session.xyDataObjects['U:Magnitude PI: ASSEMBLY N: 1_' + str(c)]
session.writeXYReport(fileName = str(a) + '-U.rpt', xyData=(U0, ), appendMode=OFF)
```

```
CF0 = session.xyDataObjects['CF:Magnitude PI: ASSEMBLY N: 1_' + str(c)]
session.writeXYReport(fileName = str(a) + '-CF.rpt', xyData=(CF0, ), appendMode=OFF)
```

C
Matlab Code

```
%=================================================================
% Residual Tension in a pure bending specimen
% Autor:  Verônica Miquelin Machado
%=================================================================
clc;
clear;

%Specimen cross section data
t=5; %thickness
A=25; % Distance between supports in the 4 point bending
W=15; %width

E = 200000; %Young's Modulus

%Maximum Deformation:
emax=0.0001;

%Number of cross-section parts
Num=50;

%Initializing variables
Mc=0;
Md=0;
ec=zeros(1,Num+1);
Sc=zeros(1,Num+1);
epc=zeros(1,Num+1);
alphac=zeros(1,Num+1);
yc=zeros(1,Num+1);
ed=zeros(1,Num+1);
Sd=zeros(1,Num+1);
epd=zeros(1,Num+1);
alphad=zeros(1,Num+1);
yd=zeros(1,Num+1);

% Loading
for i=2:(Num+1)     [e1,S1,ep1,alpha1,n1] =
PCCarregamento(0,0,0,0,0.000001,emax*(i1)/Num,1);
        ec(i)=e1(n1-1);
        Sc(i)=S1(n1-1);
        epc(i)=ep1(n1-1);
        alphac(i)=alpha1(n1-1);
        %Cross-section point coordinate
        yc(i)=((i-1)*t)/(2*Num);
        %Integration for moment calculation
        Mc=Mc+2*W*(t/(4*Num))*(Sc(i-1)*yc(i-1)+Sc(i)*yc(i));
end
```

```
%Applied load:
Pc=Mc/A;
efinal=ec(Num+1)-(6*Mc)/(E*W*t^2);

%Unloading
for j=2:(Num+1)     [e2,S2,ep2,alpha2,n2] =
PCDescarregamento(ec(j),epc(j),alphac(j),Sc(j),0.000001,efinal*(j1)/Num,n1-1);
        ed(j)=e2(n2);
        Sd(j)=S2(n2);
        epd(j)=ep2(n2);
        alphad(j)=alpha2(n2);
        %Cross-section point coordinate
        yd(j)=((j-1)*t)/(2*Num);
        %Integration for moment calculation
        Md=Md+2*W*(t/(4*Num))*(Sd(j-1)*yd(j-1)+Sd(j)*yd(j));
end

%Applied load:
Pd=Md/A;

x=zeros(1,Num+1);
v=zeros(1,Num+1);

figure
hold on
plot(ec,yc,'o-')
plot(-ec,-yc,'o-')
title('Deformação na seção transveral depois do carregamento')
grid on
hold off

figure
hold on
plot(Sc,yc,'o-')
plot(-Sc,-yc,'o-')
title('Tensão na seção transversal depois do carregamento')
grid on

figure
hold on
plot(Sd-Sc,yd,'o-')
plot(-Sd+Sc,-yd,'o-')
title('Tensão no descarregamento')
hold off
grid on

figure
hold on
```

```
plot(ed,yd,'o-')
plot(-ed,-yd,'o-')
title('Deformação residual após o descarregamento')
hold off
grid on

figure
hold on
plot(Sd,yd,'o-')
plot(-Sd,-yd,'o-')
title('Tensão residual após o descarregamento')
hold off
grid on

e=zeros(1,n2);
S=zeros(1,n2);

for cont=1:n1
        e(cont)=e1(cont);
        S(cont)=S1(cont);
end

for cont=(n1+1):n2
        e(cont)=e2(cont);
        S(cont)=S2(cont);
end

figure
plot(e,S,'r')
title('Curva Tensão x deformação')
grid on


function [ef,Sf,epf,alphaf,nf] = PCCarregamento(ei,epi,alphai,Si,dei,efi,ni)
syms a

%Stressx strain curve
H0=450;
HL=129.24;
Hinf=715;
b=50;
Sy(a)=H0+HL*a+(Hinf-H0)*(1-exp(-b*a));

K(a)=diff(Sy);
E = 200000;

i=ni;
%Initial condition
```

```
e(i)=ei;
ep(i)=epi;
alpha(i)=alphai;
S(i)=Si; de=dei;

%Return-Mapping code
while e(i) <= efi
        %1st phase
        e(i+1)=e(i)+de;
        ep(i+1)=ep(i);
        alpha(i+1)=alpha(i);
        S(i+1) = S(i)+E*de;
        f=abs(S(i+1))-Sy(alpha(i+1));
        gaman=0;
        if f>0
                Sn=S(i);
                alphan=alpha(i);
                gaman=NRgama(E,Sn,alphan,de);
                Cep=E-((E^2)/(E+K(alphan)));
                Snb=Sn+Cep*de;
                ep(i+1)=ep(i)+gaman*sign(Snb);
                alpha(i+1)=alpha(i)+gaman;
                S(i+1)=S(i+1)-E*gaman*sign(Snb);
        end
        i = i + 1;
end

ef=e;
Sf=S;
epf=ep;
alphaf=alpha;
nf=i;

function [ef,Sf,epf,alphaf,nf] = PCDescarregamento(ei,epi,alphai,Si,dei,efi,ni)

syms a

H0=450;
HL=129.24;
Hinf=715;
b=50;
Sy(a)=H0+HL*a+(Hinf-H0)*(1-exp(-b*a));

K(a)=diff(Sy);
E = 200000;

i=ni;
%Initial condition
```

```
e(i)=ei;
ep(i)=epi;
alpha(i)=alphai;
S(i)=Si; de=-dei;

%Return-Mapping code
while e(i) >= (efi)
        %1st phase
        e(i+1)=e(i)+de;
        ep(i+1)=ep(i);
        alpha(i+1)=alpha(i);
        S(i+1) = S(i)+E*de;
        f=abs(S(i+1))-Sy(alpha(i+1));
        gaman=0;
        if f>0
                Sn=S(i);
                alphan=alpha(i);
                gaman=NRgama(E,Sn,alphan,de);
                Cep=E-((E^2)/(E+K(alphan)));
                Snb=Sn+Cep*de;
                ep(i+1)=ep(i)+gaman*sign(Snb);
                alpha(i+1)=alpha(i)+gaman;
                S(i+1)=S(i+1)-E*gaman*sign(Snb);
        end
        i = i + 1;
end

ef=e;
Sf=S;
epf=ep;
alphaf=alpha;
nf=i;


%Newton-Rapshon
function [gama] = NRgama(E,S,alpha,de)

syms g a

H0=450;
HL=129.24;
Hinf=715;
b=50;

Sy(a)=H0+HL*a+(Hinf-H0)*(1-exp(-b*a));

%f=0
f=abs(S+E*de-E*g*sign(S))-Sy(alpha+g);
```

```
%f'
flinha=diff(f,g);

%Parameters
x(1)=0;
tol=0.00000000001;
dx=1000;
i=1;

while dx>tol;
        x(i+1)=x(i)-vpa(subs(f,g,x(i)))/vpa(subs(flinha,g,x(i)));
        dx=x(i+1)-x(i);
        f=eval(abs(S+E*de-E*x(i+1)*sign(S))-Sy(alpha+x(i+1)));
        i=i+1;
end

gama=x(i);
```